

Title

A new numerical model for understanding free and dissolved gas progression towards the atmosphere in aquatic methane seepage systems

Authors

Pär Jansson¹, Bénédicte Ferré¹, Anna Silyakova¹, Knut Ola Dølvén¹, Anders Omstedt²

¹CAGE-Centre for Arctic Gas Hydrate, Environment and Climate, UiT the Arctic University of Norway in Tromsø, Department of Geosciences, Tromsø, Norway.

²Department of Marine Sciences, University of Gothenburg, Box 460, SE-405 30 Göteborg, Sweden

Corresponding author

Pär Jansson. Centre for Arctic Gas Hydrate, Environment and Climate

UiT – The Arctic University of Norway. Department of Geoscience

N-9037, Tromsø, Norway; Tel: +47 77646398; per.g.jansson@uit.no; <https://cage.uit.no/>

Running head

Marine 2 Phase Gas model in 1 dimension

Keywords

Methane, Gas, Model, Bubbles, Dissolution, Arctic Ocean

Abstract

We present a marine two-phase gas model in one dimension (M2PG1) resolving interaction between the free and dissolved gas phases, and the gas propagation towards the atmosphere in aquatic environments. The motivation for the model development was to improve the understanding of benthic methane seepage impact on aquatic environments, and its effect on atmospheric greenhouse gas composition. Rising, dissolution and exsolution of a wide size-range of bubbles comprising several gas species are modelled simultaneously with the evolution of the aqueous gas concentrations. A model sensitivity analysis elucidates the relative importance of process parameterizations and environmental effects on the gas behaviour. The parameterization of transfer velocity across bubble rims has the greatest influence on the resulting gas distribution and bubble sizes are critical for predicting the fate of emitted bubble gas. High salinity increases the rise height of bubbles while temperature does not significantly alter it. Vertical mixing and aerobic oxidation play insignificant roles in environments where advection is important. The model, applied in an Arctic Ocean methane seepage location, showed good agreement with acoustically derived bubble rise heights and in-situ sampled methane concentration profiles. Coupled with numerical ocean circulation and biogeochemical models, M2PG1 could predict the impact of benthic methane emissions on the marine environment and the atmosphere on long time scales and large spatial scales. Because of its flexibility, M2PG1 can be applied in a wide variety of environmental settings and future M2PG1 applications may include gas leakage from seafloor installations and bubble injection by wave action.

Introduction

The importance of natural and anthropogenic methane (CH₄) emissions to the atmosphere has been increasingly recognized in the last few decades as CH₄ contributes to greenhouse warming by about 20% (Edenhofer et al., 2014; Pachauri et al., 2014), and because CH₄ is 32 times more potent than CO₂ in terms of warming potential (Pachauri et al., 2014).

Large CH₄ reservoirs in the form of hydrates, a crystalline structure comprising water molecules encapsulating guest molecules such as CO₂ and hydrocarbons, (Sloan and Koh, 2007) exist in sediments along continental margins worldwide. They are presently estimated to contain 1800 Gt of carbon (Ruppel and Kessler, 2016), equivalent to one-sixth of the global mobile carbon pool. Hydrates are stable under high pressure and low temperature, suggesting that bottom water warming potentially dissociates hydrates at the boundary of their stability (Westbrook et al., 2009). Yearly global flux of CH₄ to the atmosphere associated with dissociation of hydrate deposits is presently estimated at 6 Tg, which amounts to less than 1% of the total CH₄ flux to the atmosphere (Kirschke et al., 2013), but hydrate dissociation rates may increase as ocean bottom water temperatures increase over human time scales (Ferré et al., 2012).

A substantial amount of CH₄ is also found trapped where permafrost (water ice that is frozen all year) caps exist. Gaseous CH₄ trapped under hydrate- and permafrost caps is presently released to through the water column to the atmosphere on the East Siberian Shelf as the caps become more and more permeable due to thawing (Shakhova et al., 2010). In the light of a rapidly warming Arctic Ocean, it is therefore crucial to understand the transport mechanisms of CH₄ from the seabed through the water column and potentially to the atmosphere in order to estimate the impacts of seafloor CH₄ emissions on the climate and the environment.

CH₄ in sediments may be present as hydrates, free (bubbles) and/or dissolved gas in pore water. CH₄ percolating upwards is subject to anaerobic oxidation within the sulphate-methane transition zone (Boetius and Wenzhöfer, 2013) but in high-velocity fluid flow systems, both dissolved CH₄ and bubbles can bypass this filter (Luff et al., 2004; Panieri et al., 2017).

After being released from the seafloor, most of the CH₄ contained in bubbles dissolve in the water column as the bubbles ascend towards the sea surface. Numerical bubble models predict that gas exchange occurs across the bubble rims and a majority of the CH₄ initially present within the bubbles dissolve near the seafloor (Leifer and Patro, 2002; McGinnis et al., 2006). Subsequently, dissolved CH₄ diffuses, is advected by ocean currents away from its source, and is, at least partly oxidized in the presence of methanotrophic bacteria (Damm et al., 2005; Uhlig and Loose, 2017). Biastoch et al., (2011) modelled the effect of microbial CH₄ oxidation on ocean acidification and showed that the ocean pH could decrease by as much as 0.25 units in a 100-year period in some areas of the Arctic Ocean. At shallow water depths, bubbles may transport CH₄ to the upper mixed layer of the ocean, where the now-dissolved CH₄ may be ejected to the atmosphere by diffusive equilibration. Shakhova et al., (2014) reported a significant reduction of dissolved CH₄ concentration in the water column on the shallow East Siberian Arctic Shelf (water depth <50 m) directly after two storm events, suggesting that diffusive emission of CH₄ to the atmosphere was enhanced by the strong vertical mixing induced by the storms. However, large CH₄ emissions from the seafloor at a slightly deeper site (~90m) west of Svalbard in the summer of 2014, did not contribute to increased CH₄ concentration in the atmosphere

(Myhre et al., 2016). Although the acoustic signature of bubble streams was observed to reach close to the sea surface, only traces of the high CH₄ concentration near the seafloor was observed near the surface. This effect was attributed to efficient gas exchange across bubble rims and the presence of a pycnocline was suggested to inhibit vertical turbulent transport of dissolved CH₄ toward the sea surface and atmosphere.

The motivation for this study was to improve the understanding of the role of the hydrosphere in locations where CH₄ is leaking from the seafloor. Specifically, the vertical distribution of free and aqueous CH₄ resulting from seafloor seepage is of great interest in order to assess potential release of CH₄ to the atmosphere and biochemical changes in the aquatic habitat.

In order to predict the fate of CH₄ or any other kind of gas, contained in bubbles in the water column, it is necessary to consider interaction with other kinds of existent gas. Only simultaneous consideration of bubble dissolution and evolution of dissolved gas can allow for understanding these processes and their impact. Numerical bubble models have been developed previously, but each show limitations. Delnoij et al., (1997) developed a bubble model for a gas-liquid column, which resolves bubble-bubble interaction (bouncing and coalescence) but does not take into account gas dissolution or pressure gradients. Johansen, (2000) modelled non-ideal gas behaviour, but ignored ambient dissolved gas and only modelled CH₄. Leifer and Patro, (2002) introduced a bubble model based on empirical observations of bubble rising speeds but assumed spherical bubbles and ignored the non-ideal behaviour of gases due to pressure and temperature. McGinnis et al., (2006) provided a bubble model resolving five bubble gases, Nitrogen (N₂), Oxygen (O₂), Carbon dioxide (CO₂), Methane (CH₄) and Argon (Ar), but did not couple free and dissolved gas and did not consider multiple bubble sizes. Stepanenko et al., (2011) presented a natural process-based model for shallow lakes with the production of CH₄ in the sediment, assuming immediate escape of CH₄ to the atmosphere. Liang et al., (2011) presented a near-surface coupled bubble- and dissolved gas model but used a size spectrum of bubbles ranging from zero to only 0.8 mm, adequately assuming spherical bubbles. Vielstädte et al., (2015) developed a linearized single bubble model with three gas species (N₂, O₂, CH₄) for the North Sea, which is only valid for depths shallower than 100 meters and ignores the evolution of dissolved gases.

All of the above models depend on parameterizations of gas-, water- and bubble properties and so uncertainties associated with those are abundant. The objective of this study is to develop and verify a new numerical model, filling knowledge gaps of previous models. The major improvements of the here presented marine two-phase gas model in one dimension (M2PG1) over previous bubble models are:

1. Dissolution (gas escaping the bubble) and exsolution (gas invading the bubble) to simulate the evolution of the free gas composition of several gas species inside the bubbles.
2. Coupling of the dissolution and exsolution of bubble gas to the temporal evolution of the dissolved gas concentration in the water column.
3. Bubbles of different sizes and size-dependent shapes.

4. Non-ideal gas behaviour for changing temperature and pressure within the bubbles as they rise through the water column.
5. Calculation of pressure-, salinity-, and temperature dependent solubility of five gas species (N_2 , O_2 , CO_2 , CH_4 , and Ar).
6. Gas emission of free gas and equilibration of dissolved gas with the atmosphere.
7. Coupling with existing models resolving transport and diffusion of water properties is made possible because of the structure of the model.

To our knowledge, M2PG1 is the first model that is able to simulate free and dissolved gas simultaneously, while using multiple bubble sizes and several gas species in both free and dissolved phases. Non-ideal gas compressibility, environment-dependent solubility, and diffusivity are included in the model as well as interaction with the atmosphere of the free and dissolved phase of all included gas species. This study focuses on CH_4 seepage from the seafloor in a cold (Arctic Ocean) environment and we aim to elucidate on the relative importance of the different included process parameterizations and compare the effects of environmental conditions on the gas dynamics. We first describe the model setup and process parametrizations and subsequently detail a sensitivity analysis, comparing the importance of parameterizations of rising speed, bubble shapes and gas transfer with the importance of bubble sizes, temperature, salinity, CH_4 oxidation rates, dissolved gas concentrations, turbulent vertical mixing and water currents. The model was applied to a known CH_4 seep site West of Svalbard (e.g. Westbrook et al., 2009; Sahling et al., 2014) and a comparison between model results and acquired data is presented.

Method

We developed a numerical marine two-phase gas model in one dimension (M2PG1) to simulate the evolution of free gas (bubbles) rising through the water column while resolving interaction with dissolved gas and the ultimate exchange of gas with the atmosphere via direct bubble transport and/or equilibration with atmospheric gas species. The model incorporates pressure- temperature- and salinity dependent gas compressibility, solubility and diffusivity and simulates multi-gas and multi-size bubbles with user-defined initial gas composition and user-defined bubble size distribution (BSD). Bubbles can be released at any chosen water depth. This study focuses on the evolution of free and dissolved gases occurring after gas (CH_4) bubbles are released from the seafloor, and interaction with atmospheric and dissolved N_2 , O_2 , CO_2 , CH_4 , and Ar. The following sections describe how M2PG1 models these processes.

Model implementation

We implemented M2PG1 in PROBE, a well-documented and freely available numerical equation solver (Svensson, 1978; Omstedt, 2011) using a finite volume discretization and FORTRAN. PROBE has been successfully used for prediction of growth and melting of sea ice (Omstedt and Wettlaufer,

1992); Coupling between weather forecasting and a process based ocean model (Gustafsson et al., 1998); Frazil Ice dynamics (Svensson and Omstedt, 1998); Marine climate studies (Hansson and Omstedt, 2008); The effect of wave-dependent momentum flux (Carlsson et al., 2009) and the carbonate system in the Baltic Sea (Edman and Omstedt, 2013). The equation solver supports a process-based approach and is intended for numerical representation of the environment, and to test and build new system understanding. It is well suited for climate impact studies, resolving the vertical structure of the investigated properties of the water column. The present model can be described in two parts: 1) PROBE resolves the evolution of vertical profiles of physical and chemical parameters such as temperature, salinity, and dissolved gas of different species; 2) M2PG1 simulates the evolution of free gas bubbles. The two parts are coupled via the exchange of gas across bubble surfaces. PROBE solves the conservation equations (equation 1) for the state variables, ϕ which in this study are salinity, temperature and dissolved gas species (N_2 , O_2 , CO_2 , CH_4 , and Ar).

$$\frac{\partial \phi}{\partial t} + \frac{Q_{IN} - Q_{OUT}}{A} \times \frac{\partial \phi}{\partial z} = \frac{\partial}{\partial z} \left(\Gamma_{\phi} \frac{\partial \phi}{\partial z} \right) + \theta \phi \quad (1)$$

The first term $\left(\frac{\partial \phi}{\partial t}\right)$ represents the local (at depth z) change with time of the state variable. The second term $\left(\frac{Q_{IN}-Q_{OUT}}{A} \times \frac{\partial \phi}{\partial z}\right)$ is the vertical advection given by multiplying the vertical gradient of the state variable by the volume convergence of in- and outflows (Q_{IN} and Q_{OUT}) normalized by the domain area (A). The right-hand side shows diffusion $\left(\frac{\partial}{\partial z} \left(\Gamma_{\phi} \frac{\partial \phi}{\partial z}\right)\right)$ and local source/sink terms ($\theta \phi$). The salinity, temperature, and concentration of dissolved gas species are represented on a vertical finite volume grid. The free gas is represented in an identical vertical grid and in bubble size classes with equivalent radii ($[r - \delta r/2, r + \delta r/2]$).

Free gas (bubbles) rises through the water column at speeds mainly dependent on bubble size and shape, while the exchange of gases across the bubble rims alters the gas composition and concentration inside and outside the bubble. While previous seawater bubble models (e.g. Leifer and Patro, 2002; McGinnis et al., 2006; Vielstädte et al., 2015) were Lagrangian, i.e. simulating the evolution of a single bubble, M2PG1 uses a Eulerian, vertically oriented finite volume grid and a bubble size spectrum to simulate any number and sizes of bubbles simultaneously. This requires that bubble rising and shrinking or growing to be discretized. Figure 1 shows a diagram of the processes involved and the numerical grid where light blue indicates dissolved gas and yellow indicates free gas. Temperature and salinity are omitted in the figure for clarity. The model is integrated (moved forward in time) using the Euler method, resolving all the above-described processes simultaneously.

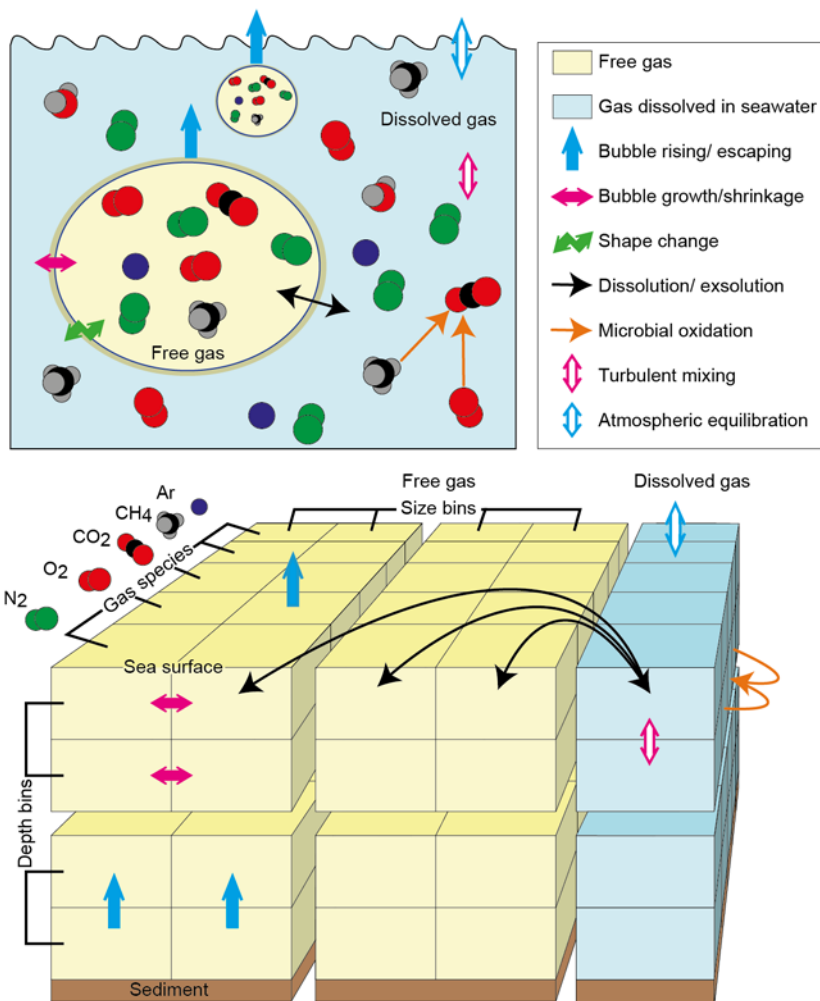


Figure 1. Diagram illustrating the physical processes involved as gas bubbles rises through the water column. Upper panel: Diagram of the natural processes occurring in the water column (blue background) and in the bubbles (yellow background). The black double arrow indicates the dissolution/ exsolution of bubble gas (transfer of different gases across the bubble rim). The solid pink double arrow shows the growth/ shrinkage of bubbles caused by pressure change and gas transfer. The green zigzag arrow indicates the shape-change of bubbles due to growth/ shrinkage. Orange arrows indicate the aerobic oxidation of CH₄, resulting in a production of CO₂ and consumption of O₂ and CH₄. The solid blue arrows represent bubble rising and the eventual free gas escape to the atmosphere. The hollow pink double arrow represents the vertical mixing of dissolved gases and the hollow blue arrow indicates equilibration of dissolved gases with the atmosphere. Lower panel: Representation of all of the above-mentioned processes in the numerical model. The left part of the grid (yellow) shows the free gas contained in depth-bins, bubble size bins and gas species, handled in M2PG1. The right (blue) part represents the dissolved gases in the same depth- and species grid mainly handled in PROBE. Arrows of the same appearance in the upper and lower panel represent the same process. For sketch simplicity, only examples of the processes are drawn (e.g., bubble rising potentially occurs between all depth bins and growth/ shrinkage occurs between all size bins).

Coupled conservation equations for free and dissolved gas

The processes constituting the source- and sink terms in equation 1 can be summarized in a set of coupled conservation equations describing the temporal evolution of free gas content and dissolved

gas concentration (equations 2 – 3, where the superscript $j \in [N_2, O_2, CO_2, CH_4, Ar]$ denotes gas species and subscripts i and k indicate indices for depth and bubble size respectively). Additional source/ sink terms at the vertical and lateral domain boundaries are given in equations 4 – 5. Notations are summarized in the supplementary information (SI.1) and each mathematical term in the equations are described in the following sections.

$$\frac{\partial n_{i,k}^j}{\partial t} = \frac{\partial n_{R,i,k}^j}{\partial t} + \frac{\partial n_{D,i,k}^j}{\partial t} \quad (2)$$

$$\theta_i^{N_2} = - \left(\frac{\sum_k^{NSBIN} \partial n_{D,k}^{N_2} / \partial t}{[\rho_{SW} \times A \times \delta_z]} \right)_i \quad (3a)$$

$$\theta_i^{O_2} = - \left(\frac{\sum_k^{NSBIN} \partial n_{D,k}^{O_2} / \partial t}{[\rho_{SW} \times A \times \delta_z]} \right)_i - k_{MOX} \times C_i^{CH_4} \quad (3b)$$

$$\theta_i^{CO_2} = - \left(\frac{\sum_k^{NSBIN} \partial n_{D,k}^{CO_2} / \partial t}{[\rho_{SW} \times A \times \delta_z]} \right)_i + k_{MOX} \times C_i^{CH_4} \quad (3c)$$

$$\theta_i^{CH_4} = - \left(\frac{\sum_k^{NSBIN} \partial n_{D,k}^{CH_4} / \partial t}{[\rho_{SW} \times A \times \delta_z]} \right)_i - k_{MOX} \times C_i^{CH_4} \quad (3d)$$

$$\theta_i^{Ar} = - \left(\frac{\sum_k^{NSBIN} \partial n_{D,k}^{Ar} / \partial t}{[\rho_{SW} \times A \times \delta_z]} \right)_i \quad (3e)$$

In equation 2, $\frac{\partial n_R}{\partial t}$ is the temporal evolution of free gas due to rising bubbles as visualized in Figure 2 a and quantified in the section “*Rising bubbles*”. $\frac{\partial n_D}{\partial t}$ is the free gas evolution due to bubble-dissolution visualized in Figure 2 b and detailed in the section “*Exchange of free and dissolved gas across bubble rims*”. In equations 3 a – e, $\left(\frac{\sum_k^{NSBIN} \partial n_{D,k}^j / \partial t}{[\rho_{SW} \times A \times \delta_z]} \right)_i$ is the dissolved gas concentration change corresponding to the dissolution occurring in all bubble sizes. Removal of CO_2 and CH_4 and production of CO_2 by aerobic CH_4 oxidation is represented by the second term in 3b, c and d (i.e. $\pm k_{MOX} \times C_i^{CH_4}$ e.), as illustrated in Figure 1 and quantified in the section “*Aerobic oxidation of CH_4* ”. Free gas content and dissolved gas concentrations are integrated forward in time simultaneously with temperature and salinity, starting with initial conditions and forced by boundary conditions.

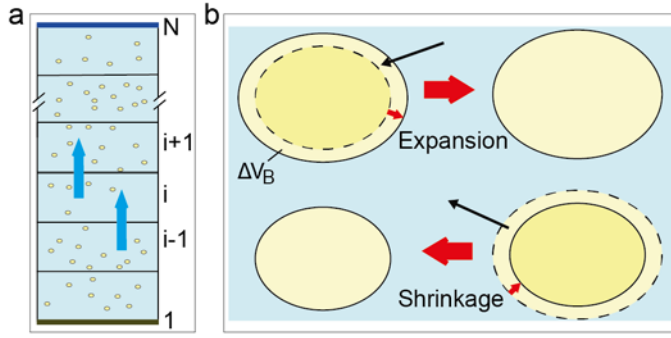


Figure 2. Representation of bubbles rising, expanding, and shrinking. a) Vertical grid with indices starting from 1 at the seafloor and up toward the surface bin, N. Ellipses illustrate bubbles within each depth bin and blue arrows indicate bubbles rising to the current bin from below and rising up to the next higher bin. b) Bubbles shrinking or expanding as described in the text. The volumetric difference between bubbles in adjacent size bins is indicated by ΔV_B and small red arrows. Bubbles are assumed oblate spheroids. Here, a denotes the length of the horizontal (semi-major) axis and b denotes the length of the vertical (semi-minor) axis.

Initial- and boundary conditions

Supplementary to the local sources and sinks, free gas content and dissolved gas concentration are affected by fluxes across the domain boundaries. Equation 4 describes the source- and sink terms of free gas at the vertical boundaries and equation 5, the source- and sink terms of dissolved gas at the lateral and vertical boundary. It is assumed that there is no dissolved gas emitted from the seafloor and no free gas is transported from beyond the lateral boundary.

$$\frac{\partial}{\partial t} (n_{i \in [bot, surf], k}^j) = Q_{EF_k}^j - Q_{AF_k}^j \quad (4)$$

$$\theta_{B_i}^j = Q_{IN_i} \times C_{B_i}^j - Q_{OUT_i} \times C_{SW_i}^j - \left(\frac{Q_{AEQ_i}^j}{\rho_{SW_i} \times A_i \times \delta_{z_i}} \right)_{i=surf} \quad (5)$$

In equation 4, Q_{EF} represents the emitted free gas (here CH_4 bubbling from the seafloor) and Q_{AF} is the bubble gas escaping to the atmosphere from the sea surface. In equation 5, $(Q_{IN_i} \times C_{B_i}^j - Q_{OUT_i} \times C_{SW_i}^j)_i$ is the concentration change due to the lateral transport of dissolved gas j in and out of the model domain. Q_{IN_i} and Q_{OUT_i} are the volumetric in- and outflow respectively from the boundary at depth $z(i)$, C_{B_i} is the concentration at the boundary and C_{SW_i} is the concentration in the modelled

water column. $\left(\frac{Q_{AEQ}^j}{\rho_{SW} \times A \times \delta_z} \right)_{i=surf}$ represents the concentration change due to equilibration of dissolved

gas j with the atmosphere, where Q_{AEQ} is the amount of gas emitted per time unit, ρ_{SW} is the seawater density calculated from temperature and salinity according to Fofonoff, (1985), and A and δ_z are the horizontal area and vertical extent of the model cell respectively. The built-in functionality of PROBE handles fluxes of heat and salinity across the boundary, using the boundary salinity and temperature in conjunction with the in- and outflow.

As bubble-dynamics depend on temperature, salinity and dissolved gas concentration in the water column, initial- and boundary conditions include vertical profiles of the modelled gas concentration and of temperature and salinity. Initial conditions are provided by the user with the same vertical resolution as the model grid (here, the profiles are 400 meters with a 1-meter resolution). M2PG1 can be forced with transient aquatic boundary conditions with vertical resolution matching the vertical grid of the forcing data and transient atmospheric boundary conditions can be specified. As the sensitivity analysis of this study aims at evaluating the influence of implemented parameters individually, we apply vertically homogenous profiles of dissolved gas, temperature, and salinity for the simulations included. The case study, on the other hand, uses measured profiles of temperature, salinity, and oxygen. Gas species, other than oxygen, are expected to be in equilibrium with the atmosphere as we lack measurements of them. The structure of the user-specified initial- and boundary conditions are listed in Table SI.7. Simulations in this analysis use static boundary conditions identical to the initial conditions.

Rising bubbles

In order to evaluate the importance of bubble rising speed on the distribution of gas in the water column, M2PG1 includes different bubble rising speed models (BRSM) that the user can select (Table SI.2). Bubbles accelerate quickly after their emission and reach terminal velocity within milliseconds when the buoyancy and drag forces balance. We therefore assume that the bubble rising speed can be derived from ambient conditions and bubble sizes, and there is no need to simulate acceleration from the moment when bubbles are released from the seafloor. The rising of gas contained in bubbles of specific sizes is discretized as visualized in Figure 2 a. The first term on the right-hand side of equation 2 describes the rate of change with time of the content of a particular gas species at depth $z(i)$ for each bubble size resulting from rising bubbles. This is quantified in equation 6, where w_b is the rising speed of the bubble.

$$\frac{\partial n_{Ri}}{\partial t} = \frac{w_{b_{i-1}} \times n_{i-1}}{\delta z_{i-1}} - \frac{w_{b_i} \times n_i}{\delta z_i} \quad (6)$$

Bubble hydrodynamics, and therefore, bubble rising speeds are influenced by surfactants on the bubble rims. Different surfactants such as bacteria (Blanchard, 1989), ions (Collins et al., 1978) and oil (Leifer et al., 2000) may contribute to immobilization of the bubble rim and can change the rising speed of bubbles. The reference case uses the BRSM suggested by Woolf, (1993) because, in spite of its simplicity, it considers both clean and surfactant covered bubbles and because the velocities are intermediate compared to other models over the relevant range of bubble sizes.

Exchange of free and dissolved gas across bubble rims

Transfer of gas molecules across bubble surfaces is a stochastic process, occurring continuously, and the net transfer is zero only when equilibrium arises between the free and the aqueous phase of all gas species simultaneously. Mass conservation requires that the sink of free gas in the bubbles, due to dissolution, $\frac{\partial n_{D_{L,k}}^j}{\partial t}$ in equation 2, is complemented by a source of dissolved gas (equations 3a – e) in the water column. This is quantified by the transfer equation (e.g. Leifer & Patro, 2002; McGinnis et al., 2006), giving the rate of change of bubble gas content resulting from dissolution/ exsolution:

$$\frac{\partial n_{D_{i,k}}^j}{\partial t} = A_{BS_{i,k}} \times \rho_{SW_i} \times k_{T_{i,k}}^j \times [C_{SW_{i,k}}^j - C_{EQ_{i,k}}^j] \quad (7)$$

In the following sections, the transfer velocity (k_T in equation 7) models (TVMs) and parameterizations of the surface area of bubbles (A_{BS}) are discussed. C_{EQ} is the dissolved gas concentration, which would result in equilibrium between the dissolved phase and the free gas inside the bubble. It is given by the solubility S and the molar fraction ($X = \frac{n^j}{\sum_1^{NGAS} n^j}$) of gas species j in the bubble according to:

$$C_{EQ_{i,k}}^j = S_{i,k}^j X_{i,k}^j \quad (8)$$

The solubility of bubble-gas in seawater depends on the total pressure inside the bubble, the temperature, and salinity of the surrounding seawater and is specific for each gas species. The pressure inside a gas bubble is affected by the hydrostatic ($P_H(z) = \int_z^0 \rho_{SW} \times g \, dz$) and atmospheric (P_{ATM}) pressures as well as the pressure induced by surface tension on the bubble interface (P_{ST_k}). The total pressure inside the bubble $P_{Bb_{i,k}} = P_{H_i} + P_{ATM} + P_{ST_k}$, where $P_{ST_k} = 2\sigma/r_{E_k}$, r_E is the equivalent bubble radius and σ is the surface tension, taken as tension between air and water. M2PG1 uses the latest parameterizations of solubilities of the included gas species (Table SI.1) that is currently available in the literature.

Gas transfer velocity

According to equation 5, the gas transfer across the bubble interface depends on the transfer velocity, k_T . Jähne et al. (1987) showed that k_T depends on the diffusion coefficient, the Schmidt number, the local small-scale turbulence, the temperature and on surfactants potentially present on the bubble rim. Numerical simulations and empirical observations have been performed, but no observation of gas transfer rates has been conducted in the deep sea and so parameterizations of k_T in natural aquatic environments are not found in the literature. Consequently, M2PG1 allows for a number of TVMs that the user can choose from, similarly to the choice of BRSM. Presently, M2PG1 includes the transfer velocity parameterization of Zheng and Yapa, (2002) for clean bubbles (TVM no. 1), parameterizations for semi-clean (TVM no. 2) and surfactant-covered (TVM no. 3) bubbles (McGinnis et al., 2006). The transfer velocity is strongly dependent on the gas diffusivity for which we rely on parameterizations listed in Table SI.1. The reference case uses the clean bubble parameterization because it produces profiles similar to observations, whereas the two other parameterizations retain gases inside the bubbles for too long. In other environmental settings, for example, where bubbles escape from oily sediments, it may be appropriate to use a TVM based on observations of surfactant-covered bubbles.

Surface areas of non-spherical bubbles

Mass transfer across the bubble rims critically depends on the surface area of bubbles (equation 5) and earlier bubble models (Leifer and Patro, 2002; McGinnis et al., 2006) assumed spherical bubbles. However, it is known that larger bubbles (transition around 1 mm radius) most often have oblate-like shapes (e.g. Rehder et al., 2002; Leblond et al., 2014). M2PG1 includes two parameterizations of bubble flatness, $f \equiv a/b$, where a and b are the semi major and semi minor axis respectively (Figure 2

b). The first parameterization follows Leblond et al., (2014) who suggest that bubble flatness is a function of the semi-major axis length and found a logarithmic relation by regression: $f = 0.45 + 1.4 \times \ln(a)$, with a in mm. This flatness parameterization is valid for $a > 1.48$ mm and smaller bubbles are assumed spherical (blue solid line in Figure 3 a). We introduce a linear flatness parametrization: $f = 1 + 0.3064a$ (blue dashed line in Figure 3 a) incorporating bubbles of small to large sizes. The surface area of an oblate spheroid, $A_{BS} = 2\pi a^2 + \frac{2\pi b^2}{\epsilon} \times \tanh^{-1} \epsilon$, where the eccentricity $\epsilon = \sqrt{1 - \frac{b^2}{a^2}}$ (Al Zaitone, 2018).

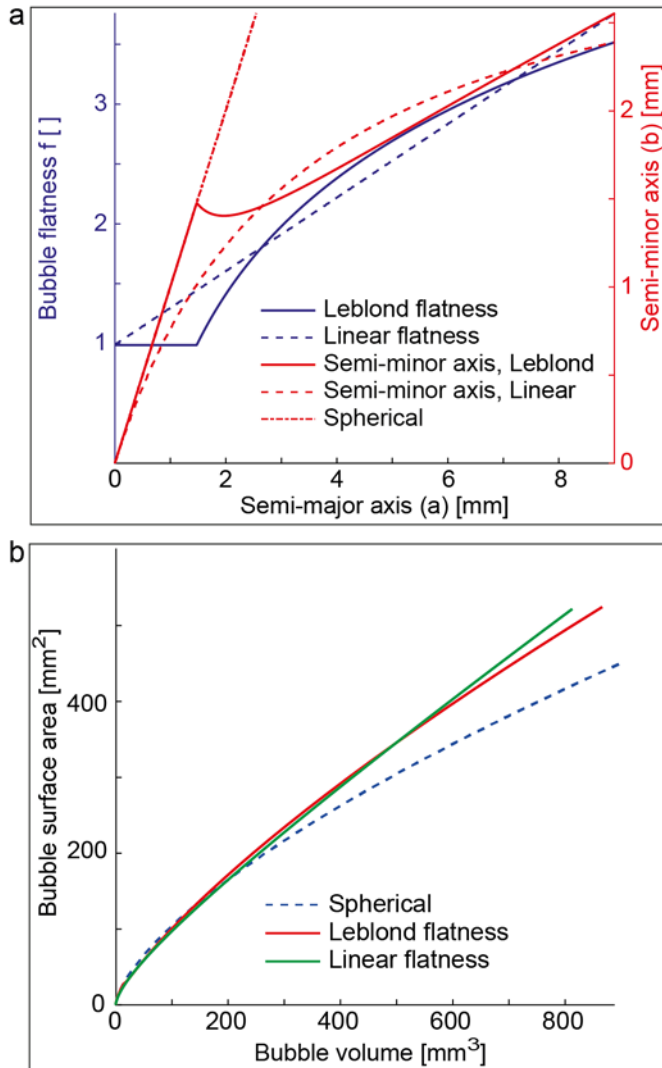


Figure 3 Three parameterizations of bubble shapes. a) The solid blue line indicates flatness as predicted by Leblond et al. (2014), dashed blue line represent the linear flatness. Red lines show the resulting semi-minor axis as functions of semi-major axis for the case of spherical (dot-line), linear flatness (dashed, this study) and Leblond flatness (solid). b) Surface area vs bubble volume as

calculated for the case of spherical bubbles (dashed blue), linear flatness (green, this study) and flatness according to Leblond (red).

The BSD is given as equivalent bubble radius, $r_E = \sqrt[3]{a^2 \times b}$ (Sam et al., 1996), requiring that M2PG1 solves for the semi-major and semi-minor axes during simulation start-up depending on the shape parameterization chosen by the user. The surface area of a flat bubble, relative to bubble volume, is larger than the surface area of a spherical bubble of the same volume (Figure 3 b).

Bubble shrinkage and expansion

Two processes affect bubble volumes simultaneously as bubbles rise through the water column: a) Gas invades or escapes bubbles depending on the dissolved gas concentrations and gas composition in the bubble. Dissolution and exsolution can occur simultaneously if the concentration of one or several gas species is supersaturated with respect to the free gas inside the bubble and another gas species is under-saturated. The bubble volume changes at rates matching the gas transfer of all gas species across the bubble rim, as indicated with black arrows in Figure 1 and Figure 2. This is quantified by $\frac{dV_D}{dt} = \sum_{j=1}^{NGAS} \frac{dn_{Dj}}{dt} \times V_{Mj}$, where V_M is the molar volume of the specific gas, calculated from ambient pressure and temperature, compliant with non-ideal gas behaviour and given by the parameterizations referenced in Table SI.1; b) Rising bubbles experience pressure- and temperature change and the volume changes according to $\frac{dV_{PT}}{dt} = \sum_{j=1}^{NGAS} \frac{w_b n^j}{\delta z} \times \Delta V_M^j$. The total temporal volumetric rate of change of rising bubbles can be written for each bubble size at each depth:

$$\frac{dV}{dt} = \frac{dV_D}{dt} + \frac{dV_{PT}}{dt} \quad (9)$$

Discretizing this process, M2PG1 moves bubble gas between bubble sizes. When bubbles shrink ($dV/dt < 0$), the gas content of species j in bubble size $k-1$ increases and the content in bubble size k will decrease with the same amount as seen in equation 10, where ΔV_B is the volumetric difference between bubble sizes and X is the molar fraction of a particular gas species.

$$\frac{dn_{k-1}^j}{dt} = \frac{\frac{dV}{dt}}{\Delta V_B} \times \frac{V_k \times X^j}{V_M^j} \quad (10)$$

$$\frac{dn_{j,k}}{dt} = -\frac{\frac{dV}{dt}}{\Delta V_B} \times \frac{V_k \times X^j}{V_M^j}$$

When bubbles grow, gas moves from size k to size $k+1$ in a similar manner. When the largest bubbles ($k=NSBIN$) are predicted to grow and smallest bubbles ($k=1$) are predicted to shrink, the gas is retained in the present bin.

Aerobic oxidation of CH₄

Aerobic oxidation of CH₄ in the water column, a biogeochemical process explicated by the chemical reaction $CH_4 + O_2 \Rightarrow CO_2 + H_2O$ implies a direct mathematical coupling between dissolved CH₄,

dissolved O₂ and CO₂. The oxidation process occurs at rates $\frac{\partial[CH_4]}{\partial t} = -k_{MOx}[CH_4]$ where k_{MOx} is the oxidation rate constant (time⁻¹) and $[CH_4]$ is the CH₄ concentration (e.g. Graves et al., 2015). Stoichiometry depicts a 1:1:1 relation between the three gas species, yielding removal rates of oxygen and production rates of carbon dioxide equal to oxidation rates of CH₄. k_{MOx} reported in the literature is typically between <0.001 and 0.7 d⁻¹ (Angelis and Scranton, 1993; Valentine et al., 2001; Mau et al., 2017). The reference simulation uses a value of 0.01 d⁻¹, which is the average constant calculated by Graves et al., (2015) at the site of our case study.

Turbulent vertical mixing

Dissolved gas in seawater, as well as heat content and salinity, are subject to vertical mixing by turbulent diffusion (e.g. Thorpe, 2007). The rate of change of the state variable (temperature, salinity, gas, or other) due to vertical diffusion is $\frac{\partial}{\partial z} \left(\Gamma \frac{\partial \phi}{\partial z} \right)$, where Γ is the vertical mixing coefficient, which can vary over several orders of magnitude. PROBE has the capability to either use a constant coefficient or calculate the coefficient according to turbulence closure schemes. Here, we apply a constant coefficient in order to isolate the effect of vertical turbulent mixing and we assume that this constant is the same for all gas species.

Atmospheric interaction

Free gas can escape to the atmosphere if bubbles reach the sea surface as seen in Figure 1. For this process, we simply assume that all bubbles reaching the surface $z(N)$ immediately escape to the atmosphere. The flow of free gas of species j to the atmosphere is, therefore, $Q_{ABj} = \sum_{k=1}^{NSBIN} n_{N,k}^j / \Delta t$, where Δt is the time-step of the model simulation.

Furthermore, dissolved gases in the water column will equilibrate with the atmosphere. The flow rate to the atmosphere is calculated according to Wanninkhof (2014):

$Q_{AEQ}^j = A \times k_A^j \times (C_{N-1}^j - C_a^j)$, where $k_A^j (cm h^{-1}) = 0.251 \times U^2 \times \left(\frac{Sc^j}{660} \right)^{-\frac{1}{2}}$, and Sc is the temperature dependent Schmidt number, calculated for the different gas species according to Wanninkhof, (1992); (2014) and U is the wind speed (m s⁻¹) at 10 meters above the sea surface. Positive rates indicate gas flow to the atmosphere.

User-specified simulation details

Environmental conditions controlling the evolution of free and dissolved gas are defined, and bubble shape parameterization, BRSM and TVM are chosen by the user together with horizontal domain area, time-step, interval for model output (detailed in Table SI.4), bubble size distribution (BSD) (Example in Table SI.5), composition of gas contained in emitted bubbles (Table SI.6), free gas flow rate and k_{MOx} . The user can choose between constant or transient mixing coefficients (applied or calculated by the model). Transient oceanic and atmospheric boundary conditions can be used to force the model. All settings are supplied by the user in an initialization file, as detailed in Table SI.7.

Assessment

Budget analysis and numerical precision

The numerical precision of M2PG1 was assessed by simulating a continuous release of $0.1 \text{ mol CH}_4 \text{ s}^{-1}$ emitted at 80 meters water depth as bubbles with 3 mm initial equivalent bubble radii (linearly flat bubbles were assumed). The residual (*res*) was defined as the initial dissolved gas content plus the sources and sinks minus the integrated current free and dissolved gas content (equation 11). A smaller residual means better numerical precision.

$$\begin{aligned} \text{res}(t) = & \overbrace{\sum_{i=1}^N ([CH_4] \times \rho_W \times \delta_z \times A)}^{t=0} \\ & + \sum_{t_m}^{t_m+\Delta t} \left[\left(Q_{EF} - Q_{AF} - Q_{AEQ} - \sum_1^{Nz} MOx \right) \times \delta t \right] - \overbrace{\sum_{i=1}^N \sum_{k=1}^{NSBIN} n_{i,k}}^t \\ & - \overbrace{\sum_{i=1}^N ([CH_4] \times \rho_W \times \delta_z \times A)}^t \end{aligned} \quad (11)$$

Here, $\overbrace{\sum_{i=1}^N ([CH_4] \times \rho_W \times \delta_z \times A)}^{t=0}$ represents the initial (t=0) content of dissolved CH₄ and

$\overbrace{\sum_{i=1}^N ([CH_4] \times \rho_W \times \delta_z \times A)}^t$ is the content at the time of the model output (every 10 minutes). The term $\sum_{t_m}^{t_m+\Delta t} [(Q_{EF} - Q_{AF} - Q_{AEQ} - \sum_{i=1}^N MOx(i)) \times \delta t]$ represents the sources and sinks at the vertical boundaries and a local sink due to oxidation. These quantities are accumulated over time, written to result-files and reset at time intervals of 10 minutes ($\Delta t=600 \text{ s}$) (t_m represents the time of the model output). The model time-step $\delta t=1/16 \text{ s}$. Q_{EF} is the free gas emission to the water columns, emitted at 80 meters water depth for the budget analysis in order to observe both free gas bubbles escaping to the atmosphere and equilibration at the sea surface. Q_{AF} is the free gas emitted into the atmosphere, Q_{AEQ} is the dissolved gas escaping to the atmosphere by means of equilibration, and MOx

is the CH₄ removal by aerobic oxidation. The double summation $\overbrace{\sum_{i=1}^N \sum_{k=1}^{NSBIN} n_{i,k}}^t$ represents the free

gas CH_4 present at the current time where n represents the free gas molar content in bin i , k . N is the number of vertical grid cells, and NSBIN is the number of bubble sizes. The residual was less than 1‰ of the total CH_4 gas content as seen in Figure 4. Thus, the numerical accuracy was better than 99.9% for the test simulation.

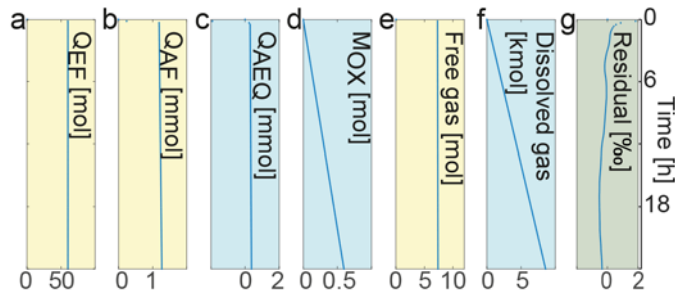


Figure 4. CH_4 budget calculated from the model output and numerical error during simulation. a) Free gas CH_4 emitted from the seafloor, accumulated over the period between model outputs. b) Escape of bubble-mediated CH_4 to the atmosphere accumulated the same way. c) Accumulated dissolved CH_4 equilibration with the atmosphere. d) Accumulated aerobic oxidation of CH_4 . e) Total free gas CH_4 content. f) Total dissolved CH_4 content. g) Residual (equation 11) divided by the total CH_4 content in the free and dissolved phase.

Model sensitivity

The model sensitivity was analysed with 53 simulations which were run to steady state, here identified when the relative integrated content difference between time-steps was less than 10^{-6} . The sensitivity analysis was performed by evaluating 1) bubble property parameterizations, 2) environmental influence on the result. Analysis of different parametrizations and environmental conditions were further divided into subgroups consisting of a number of simulations as indicated in Table 1 and detailed in the supplementary information, Table SI.8. The reference case (M2PG1 0.0) uses BRSM no. 7, TVM no. 1, linearly flat bubbles and vertically homogenous dissolved gas profiles at equilibrium with the atmosphere assuming atmospheric mixing ratios of 79% N₂, 20% O₂, 0.97% Ar, 399 ppm CO₂, and 1830 ppb CH₄, where ratios for CO₂ and CH₄ were obtained from the annual global average in 2015 (Ed Dlugokencky, NOAA/ESRL, www.esrl.noaa.gov/gmd/ccgg). It further uses a single bubble size distribution of 3 mm, which is the peak radius of the BSD observed by Veloso et al., (2015); a temperature of 4°C and a salinity of 35 PSU, which was observed near the seafloor during a cruise to the study area as described in the section *Case study*; a flow rate of 0.05 mol s⁻¹, equivalent to the mean flow rate of observed bubble streams during the same cruise; an oxidation rate constant of 0.01 d⁻¹, which is the mean oxidation rate constant determined by Graves et al., (2015) in the same area; a water current of 15 cm s⁻¹ as determined from the typical inclination of bubble streams; a vertical mixing coefficient of 0.001 m²s⁻¹, was applied, which is high compared with sparse literature data from the area (Randelhoff et al., 2015), but in the low range of oceanic values (Wunsch and Ferrari, 2004).

Table 1. Overview of simulations included in the sensitivity analysis.

	Subgroup	Target	Unit	Case settings
Bubble property parameterizations	1	Bubble rising speed	[Model no.]	1, 2, 3, 4, 5, 6, 7*, 8, 9
	2	Bubble shapes	[Model]	Spherical, Leblond, Linear*
	3	Transfer velocity	[Model no.]	1*, 2, 3
Environmental settings	4	Dissolved gas profiles	[$\mu\text{mol kg}^{-1}$]	Atmospheric equilibrium*, Half O ₂ , 1/100 O ₂ , No Argon, Double CO ₂ , No N ₂ , Double N ₂ , Tenfold N ₂
	5	Bubble size distribution**	[mm]	1, 2, 3*, 4, 6, 8
	6	Temperature	[°C]	0 ¹ , 1 ¹ , 2 ¹ , 3 ¹ , 4*, 6, 8, 10, 20
	7	Salinity	[PSU]	0, 20, 35*, 40
	8	Flow rate	[mol s ⁻¹]	0.025, 0.05*, 0.1, 0.2
	9	Oxidation rate constant	[d ⁻¹]	0, 0.01*, 0.1, 1, 10
	10	Water current	[m s ⁻¹]	0.025, 0.05, 0.1, 0.15*, 0.2, 0.5
	11	Mixing coefficient	[m ² s ⁻¹]	0.0001, 0.001*, 0.01, 1, 100, 10000

* Used in reference case; ** Single initial bubble radius; ¹ Within CH₄-HSZ

Sensitivity to bubble property parameterizations

The sensitivity analysis of the bubble property parameterizations included simulations targeting bubble rising speeds and transfer velocities (Figure 5), and a separate analysis of shape parameterizations. We compared the CH₄ profiles resulting from nine BRSMs (SI.2, Table SI.3, and Figure SI.1). The existence of surfactants on the bubble rim and its effect on the rising speed is beyond the scope of this study, and the resulting profiles do not clearly discriminate between clean and surfactant-covered BRSMs. The transfer velocity parametrizations are coupled to the rising speed of bubbles, which implies that the analysis of BRSMs and TVMs are linked. For that reason, the effect of the choice of BRSMs remains unclear. However, studies suggest that bubbles observed in natural conditions behave as surfactant covered, justifying a reference case based on a surfactant BRSM. On

the other hand, TVMs based on surfactant-covered bubbles yield unrealistic profiles and we therefore chose a clean bubble TVM for the reference case.

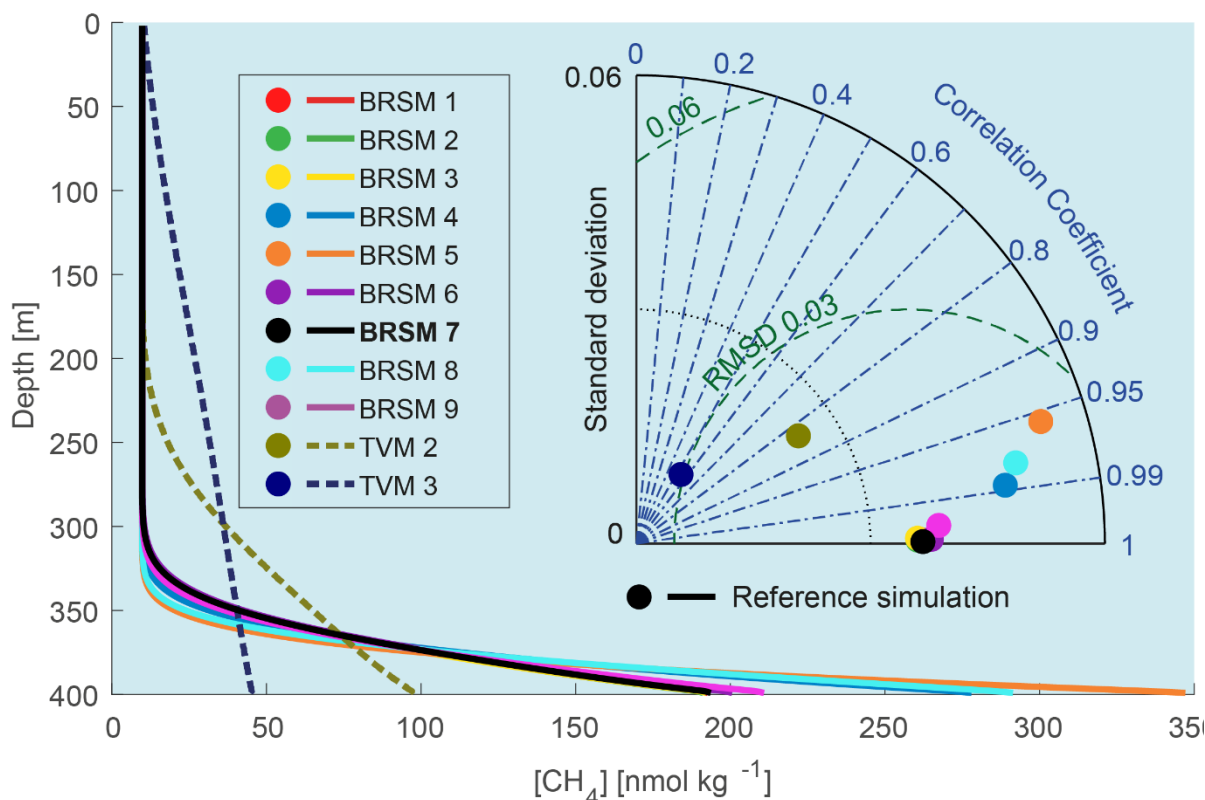


Figure 5. Simulation results targeting BRSMs (solid lines) and TVMs (dashed lines). The main graph shows dissolved CH₄ concentration profiles in the water column after simulations reached steady state. Dots in the Taylor diagram (Taylor, 2001) indicate standard deviation, correlation coefficients, and root mean square differences (RMSD) compared to the reference simulation (black line and dot) and are colour-coordinated with the profiles. The profile resulting from BRSM no. 3 was identical to the reference and is therefore hidden. The nine BRSM simulations use TVM no. 1 and the TVM simulations use BRSM no. 7.

We define the modelled flare height (equivalent to the acoustic signatures of free gas in the water column) as the height where less than a threshold fraction of the emitted gas remains. Here we consider a 10% threshold and hereafter refer to the corresponding 10% flare height. The height of the modelled flares and consequently the vertical distribution of dissolved CH₄ in the water column are affected by the choice of BRSM. Simulations show that the 10% flare height is 41% higher when BRSM no. 9 is chosen compared to when BRSM no. 5 is applied, i.e. 51.6 vs 36.6 m (Table SI.7), despite the fact that both models consider surfactant covered bubbles. The 10% flare heights in the BRSM subgroup were 49.5 ± 6.4 m and the concentration close to the seafloor in the present subgroup was $0.24 \pm 0.06 \mu\text{mol kg}^{-1}$, highlighting the importance of the choice of BRSM in the prediction of the vertical distribution of CH₄ in the water column.

Simulations using TVM for both semi-clean (TVM no. 2) and surfactant (TVM no. 3) yielded strikingly different profiles compared to the reference case (TVM no. 1). Our simulations showed that bubbles rose more than twice as high compared to the reference case with a TVM based on

intermediately surfactant-covered bubble rims. The 10% flare height of TVM no. 2 was 135.8 m compared to 54.6 m for the reference case (TVM no. 1). The surfactant based TVM (no. 3) caused bubbles to reach the surface even from 400 m water depth, which has not been observed in seep sites outside the HSZ.

The importance of the bubble flatness parameterizations was investigated using a bubble size distribution describing single size initial bubbles of 6 mm equivalent bubble radius and otherwise default settings. One case was based on the linear flatness as previously described, which is also used in our reference case; a second case used the flatness parametrization suggested by Leblond et al., (2014), and the third case assumed spherical bubbles. These simulations showed that the 10% flare height was 21% higher when spherical bubbles were applied compared to the two flat bubble parameterizations, which showed similar results (Figure 6). The dissolved CH₄ concentration profiles from these special cases had smaller gradients and the maximum concentration (close to the seafloor) was 23% lower when spherical bubbles were assumed. For 3 mm equivalent radius bubbles, the 10% flare height resulting from the spherical bubble assumption was 5% lower than the flare height of flat bubbles (Table SI.8). The simple linear flatness parameterization produced similar results to the parameterization of Leblond while avoiding the sharp flatness transition at semi-major axis at 1.48 mm and is therefore recommended (Figure 3 a).

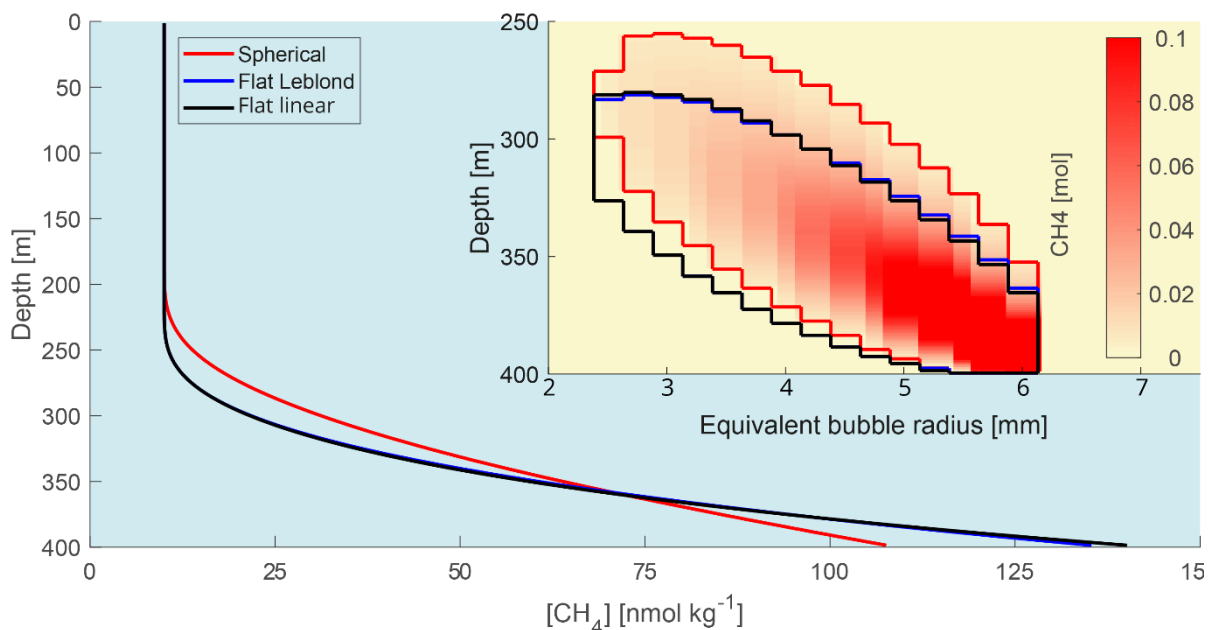


Figure 6. Modelled influence of flat bubble parameterizations. The main graph shows the steady-state profiles of dissolved CH₄ concentrations using 6 mm initial equivalent bubble radius. The red line represents the simulation with spherical bubbles. Black and blue lines show results from linear and Leblond flatness parameterizations respectively. The inset diagram shows free CH₄ gas content at steady state for the three simulations. Red colour scale and bounding polygon indicate the spherical case while black and blue polygons represent Leblond and M2PG1 parameterizations. Polygon boundaries were calculated from a 1-mmol free gas content threshold.

Model sensitivity to environmental conditions

We performed 41 simulations including the reference case with varying settings in order to evaluate the relative importance of environmental conditions (Table 1, subgroups 4 – 11) on the resulting vertical profile of dissolved CH₄. Figure 7 shows an overview of the importance of the environmental parameters. The simulation results obtained from different conditions are summarized in Table SI.8 and the results are evaluated separately in the following sections. Definitions of the correlation coefficient, root mean square difference, and standard deviations are provided in table SI.8.

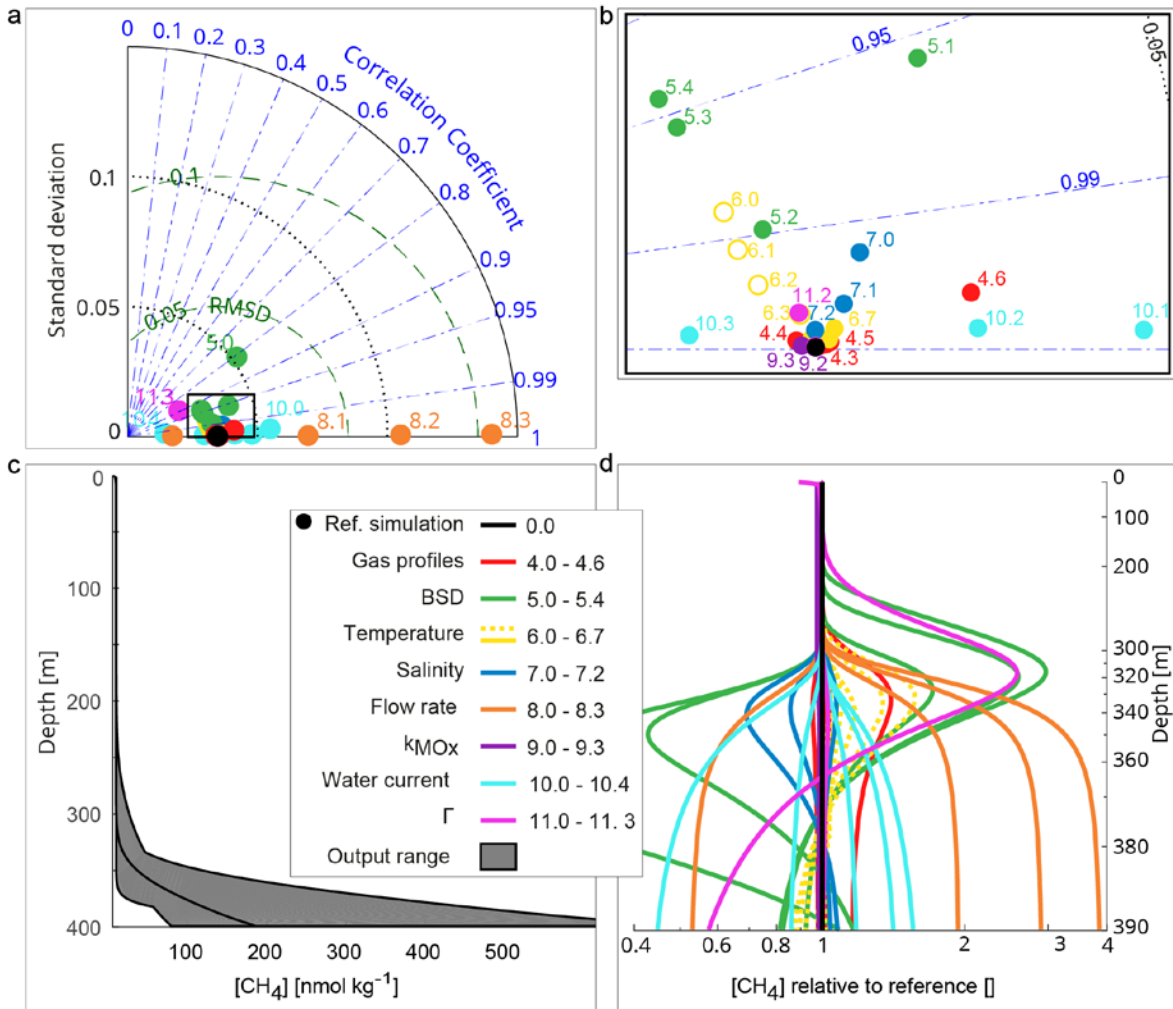


Figure 7. Modelled CH₄ profiles and statistics. a) Taylor diagram showing the standard deviation, root mean square difference (RMSD) and correlation coefficient of simulations compared to the reference case, shown in black. Red dots: varying dissolved gas profiles, green dots: varying BSD, yellow dots: varying temperature, blue dots: varying salinity, orange dots: varying flow rates, purple dots: varying oxidation rate, light blue dots: varying water current and pink dots: varying vertical mixing. b) Zoom of the black rectangle in panel a, with the same colour-coding. c) Dissolved gas vertical profiles after simulations reached steady state. Grey area shows the span of the model output for all simulations with varying environmental aspects. The reference simulation is shown as a black line. d) Steady-state profiles following the same colour coding, normalized by the reference case profile and plotted on a logarithmic depth axis. Dashed (yellow) lines indicate simulations partly within the CH₄-HSZ (see Table SI.8 for details). Simulations 11.0 and 11.1 are not seen here because they coincide with the reference simulation. Note the different depth scales of panel c and d for a more detailed visualization.

Dissolved gas profiles.

We ran seven simulations using different gas profiles (simulations 4.0 – 6; table 1 and SI.8 for details; red dots and lines in Figure 7). Small deviations from the reference case simulation result from changing the ambient dissolved gas profiles. Neither removing the Argon gas, accounting for approximately 1% of the atmospheric gas composition nor reducing the oxygen concentration by 99% changed the rise height of the CH₄ plume. An improbable tenfold increase in N₂ increased the 10% flare height by 13 meters. Simulations suggest that the initial and boundary dissolved gas concentrations within plausible ranges do not significantly influence the rise height of free gas in environments where the water mass is well ventilated like in all our cases.

Bubble size distribution

An important feature of M2PG1 is its capability to simulate bubbles with a range of bubble sizes, which is typically observed in natural seep systems. However, in order to isolate the effect of different bubble sizes, it was necessary to simplify the size distribution and simulate the release of bubbles, of initially one size. Five single-size bubble simulations were performed (simulations 5.0 - 4; 1, 2, 4, 6, 8 mm equivalent bubble radii; green dots and lines in Figure 7) which showed that the size of bubbles escaping from the seafloor strongly affects the vertical distribution of dissolved CH₄. Compared to 3 mm bubbles (our reference), the 10% CH₄ plume was lower by 57% when 1 mm bubbles were assumed and was higher by 87% when an 8 mm equivalent bubble radius was applied. Small bubbles have the capacity to increase the near-seafloor concentration because they dissolve quickly and rise slowly. – For example, 1 mm bubbles increased the bottom water concentration by 230% compared to 3 mm bubbles.

Temperature

Simulations using eight vertically homogenous temperature profiles (simulations 6.0 – 7; 0 – 3, 6, 8, 10, 20°C) are shown as yellow dots and lines in Figure 7. Bubbles within the HSZ become covered with hydrate skins (e.g. Sauter et al., 2006), but the growth rate of hydrates on bubble rims and their influence on the gas transfer velocity and rising speed are largely unknown and therefore not implemented in this version of M2PG1. Simulations 6.0 – 6.3 with temperatures, $T \in [0, 1, 2, 3] \text{ } ^\circ\text{C}$, are partly within the HSZ and therefore unreliable. To isolate the temperature effect on bubble dynamics, we performed an additional 18 simulations (not shown in Table 1 or SI.8) with the release of CH₄ bubbles from 100 and 200 m water depths, where CH₄ hydrates are unstable at all temperatures. We observe a weak trend towards higher plume heights with higher temperatures (Figure 8), to which we attribute the lower solubility associated with warmer water.

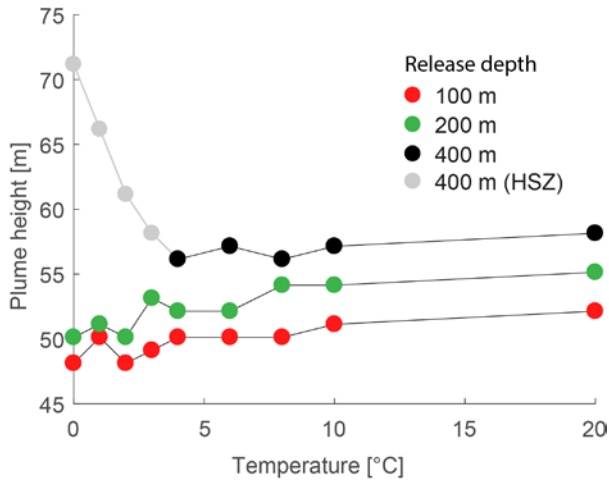


Figure 8. Temperature-dependent dissolved CH₄ plume heights. Plume heights are calculated as the height where the concentration anomaly is less than 10% of the maximum anomaly. Red, green, and black dots represent plume heights from bubbles released at 100, 200, and 400 m respectively. Grey dots indicate that the bubbles are partly within the CH₄-HSZ and therefore represent unrealistic results.

Salinity

Simulations using three different vertically homogenous salinity profiles (simulations 7.0 – 2; 0, 20, 40 PSU) confirm that high salinity causes gas to rise higher. The 40 PSU salinity causes the CH₄ plume to reach 12% higher compared to the 20 PSU case and 21% higher compared to the fresh-water case. This is explained by the lower solubility of CH₄ caused by salts in the water. The plume height difference between the 35 PSU case and the fresh-water case was 12 meters (14%).

Flow rate

Any change in flow rate (simulations 8.0 – 3; 0.025, 0.1, 0.15, 0.2 mol s⁻¹) simply results in an absolute concentration shift. The shape of the dissolved CH₄ profiles (orange dots and lines in Figure 7) did not change due to changed flow rates. This stems from the fact that the modelling approach does not consider bubble-bubble interaction or upwelling flow caused by bubbles.

Aerobic CH₄ oxidation rate constant

Five different simulations, using different values of the oxidation rate constant, k_{MOx} (simulations 9.0 - 3; 0, 0.01, 0.1, 1, 10 d⁻¹), yield profiles with a near-perfect match. This implies that aerobic oxidation of CH₄ is negligible on time scales given by relatively strong water currents and small domain sizes: in the simulations, we consider a domain of 1800 m², equal to the echosounder beam area of 25 m radius and a default water current of 15 cm s⁻¹, yielding a residence time of 5 minutes, which for $k_{MOx} = 1 \text{ d}^{-1}$ would remove less than 5 ‰ of the present.

Water currents

Five simulations addressing the effect of advection through ocean currents (simulations 10.0 – 4; 0.025, 0.05, 0.1, 0.2, 0.5 m s⁻¹; cyan dots in Figure 7) were performed. The profiles of all state variables at the lateral boundary were vertically homogenous throughout our sensitivity simulations and the inflow of dissolved gas nudged the concentration profiles toward the boundary level. Therefore, profiles resulting from strong currents were more similar to the boundary profiles. Specifically, CH₄ profiles displayed smaller gradients and lower concentrations for cases with stronger currents. Plume heights were higher for stronger water currents but not higher by absolute concentrations (Table SI.8). This is consistent with the fact that the ambient concentrations did not affect the bubble rise heights significantly.

Vertical mixing

Wunsch and Ferrari, (2004) reported on oceanic vertical diffusion coefficients ranging from $3 \times 10^{-4} - 500 \times 10^{-4} \text{ m}^2 \text{ s}^{-1}$. A plausible low eddy diffusion coefficient (simulation 11.0; $10^{-4} \text{ m}^2 \text{ s}^{-1}$) did not influence the vertical distribution of dissolved CH₄ and neither did a high coefficient (simulation 11.1; $1 \text{ m}^2 \text{ s}^{-1}$). A mixing coefficient of $100 \text{ m}^2 \text{ s}^{-1}$, represented by the pink dot (11.2) and hardly visible pink line in Figure 7, only slightly changed the profile. The vertical profile was noticeably altered by the high-end mixing coefficient (simulation 11.3; $10^4 \text{ m}^2 \text{ s}^{-1}$) but such strong vertical mixing is not observed in the ocean. The vertical mixing of dissolved gas is thus negligible in environments where ocean currents carry the dissolved methane away from the source. The fate of seeped methane is only marginally dependent on vertical mixing even away from the source area (Graves et al., 2015) unless turbulence is particularly enhanced.

Case study

We performed a three-day ship-based survey at a known CH₄ seepage site (e.g. Westbrook et al., 2008; Sahling et al., 2014) on the continental slope west of Svalbard in October 2015 (Figure 9 a), where we acquired continuous echosounder data (EK60 operated at 18 and 38 kHz). Flares were inferred from the echosounder data and were observed to rise up to 50 – 150 meters above the seafloor. We performed three Conductivity-Temperature-Depth (CTD) hydrocasts including discrete

water samples in the close vicinity of gas flares (see Figure 9a for locations). Water samples were analysed for dissolved CH_4 concentrations following the headspace gas chromatography method described by Magen et al., (2014). A continuous exponential function was fitted to the discrete CH_4 concentration data and was subsequently used for comparison with model simulations (Figure 9 e).

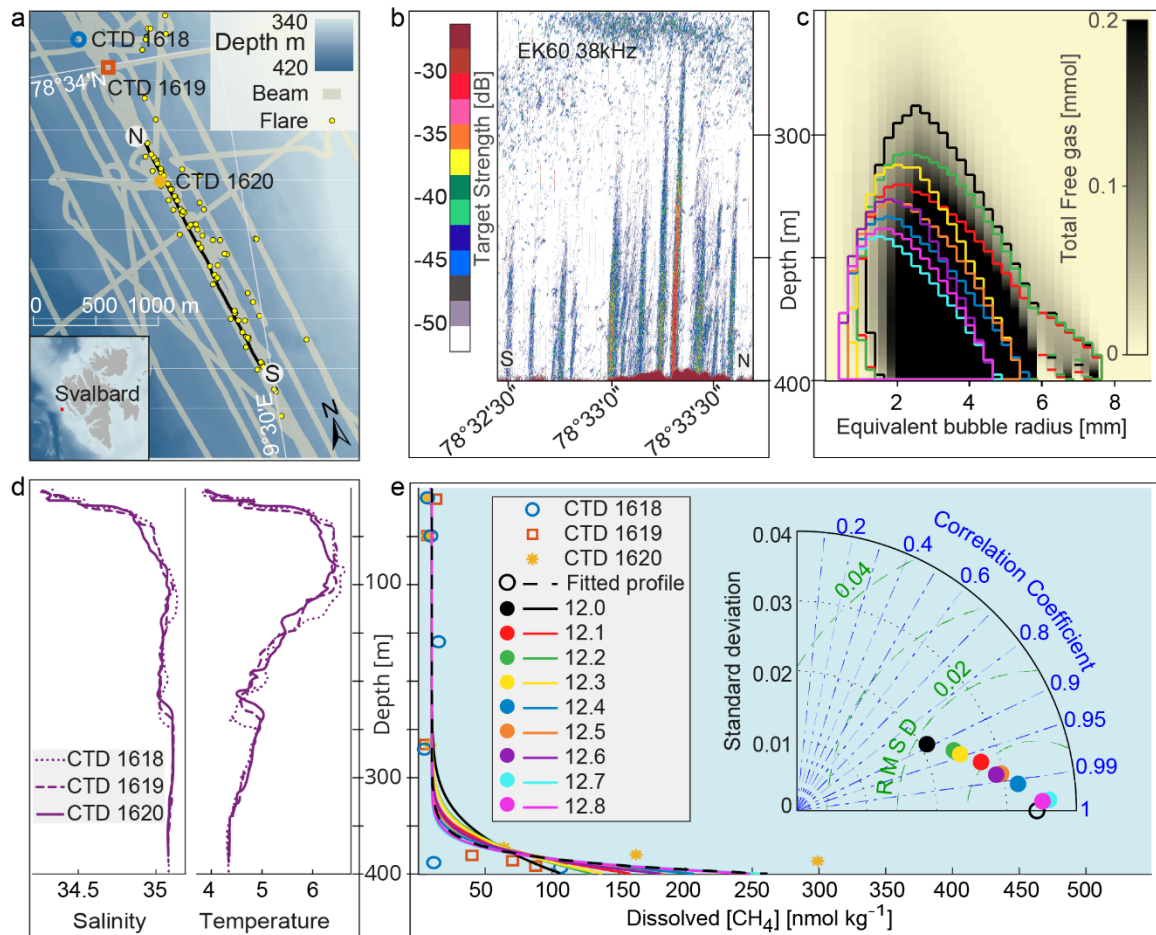


Figure 9. Case study compared to model simulations. a) Map of the case study area showing identified flares (yellow dots), echosounder beam coverage (grey lines), the transect shown in panel b (black line delimited by labels S and N) and CTD cast locations (blue ring (CTD 1618), red square (CTD 1619), and orange star (CTD 1620), referred to in panel d and e). b) Echosounder data acquired from the ship mounted EK60 operated at 38 kHz on October 22, following the track from S to N in panel a. Colours indicate the target strength (dB) – an indicator for the quantity of free gas (bubbles) in the water. c) Grey to black shades indicates the modelled content of free gas (all species) at steady state of simulation 12.0 and its distribution in bubble size- and depth bins. Coloured contour lines indicate the limit where the free gas exceeds 0.05 mmol. Contours for model simulations are colour coded accordingly with the legend in panel e. d) Salinity and temperature profiles of performed CTD casts. e) Discrete CH_4 concentrations acquired from CTD casts and subsequent Gas Chromatograph measurements shown with symbols matching panel a. A continuous dissolved CH_4 profile function, fitted to the discrete data is shown as a dashed black line. Steady state model output profiles are shown as lines with the same colour coding as panel c. Inset Taylor diagram summarizes the correlation coefficient, standard deviation, and root mean square difference between the fitted profile and the model simulations (equations in Table SI.7). Dots in the Taylor diagram are colour coded accordingly with the legend.

We performed nine simulations using the temperature- and salinity data from the three CTD casts (Figure 9 d). For simulations 12.0 – 12.2 we used a Gaussian-like BSD peaking at 3mm equivalent bubble radius which was observed in the area in 2011 and 2012 (Veloso et al., 2015). Simulations 12.3 – 12.5 were set up with smaller bubbles (peak radius of 2 mm) and 12.6 – 12.7 were set up with 1 mm peak radius. The water current was estimated to 18.5 cm s^{-1} based on the inclination of flare spines calculated with the FlareHunter software (Veloso et al., 2015). BRSM no. 7 was used in simulations 12.0, 12.3 and 12.6; BRSM no. 5 was used in 12.1, 12.4, and 12.7; no. 8 was used 12.2, 12.5, and 12.8.

The observed acoustic flare heights (Figure 9 b) were well reproduced by the nine M2PG1 simulations (Figure 9 c and Table SI.7). The simulated rise heights of gas bubbles obtained with the 3 mm peak radius BSD almost matched the highest observed flares while the bubble rise heights obtained from simulations 12.3 – 12.7 (Gaussian BSDs with 2 and 1 mm peak radii) matched the height of the lower flares (Figure 9 b and Figure 9 c). Simulated dissolved CH_4 profiles correlated well ($r > 0.9$) with the fitted function and the root mean square difference (RMSD) was less than $0.02 \mu\text{mol kg}^{-1}$. The simulations using 3 mm peak radius bubbles show that the modelled dissolved CH_4 concentrations near the seafloor were lower than the concentrations of the fitted curve, but above approximately 15 meters, the simulated concentrations were higher (Figure 9 e). The small bubble simulations (12.7 and 12.8) produced dissolved methane profiles almost identical with the fitted function based on observations. We calculated TS values according to equations 1 – 9 Veloso (2015) by integrating the backscatter area of the simulated bubbles at steady state and we defined TS heights as the height where the simulated TS dropped below -55 dB (Value used for discriminating between gas and water). The resulting heights were 60 – 102 meters above the seafloor for the included cases and were 158 – 183 m for additional simulations using 5 – 8 mm Gaussian BSDs.

Discussion and conclusion

We developed a marine two-phase numerical model in one dimension (M2PG1) that simulates the dynamics of free and dissolved gases in the water column. To our knowledge, it is the first model that simulates the two gas phases simultaneously, with multiple bubble sizes comprising multiple gases. M2PG1 considers non-ideal gas behaviour, pressure- temperature- and salinity dependent solubility and diffusivity. M2PG1 resolves direct bubble-mediated gas escape to the atmosphere as well as diffusive flow of dissolved gas through equilibration with the atmosphere. The model also simulates aerobic oxidation, converting CH_4 into carbon dioxide while consuming oxygen. The numerical accuracy of the model was better than 99.9%, which, in spite of the more complex calculations, is comparable with the model developed by Vielstädte et al., (2015). Predicting the fate of bubble gas in the water column requires knowledge of the sizes and gas composition of the bubbles, water currents, initial-, and boundary conditions of salinity, temperature, and dissolved gas species. Moreover, parameterizations of bubble shapes, rising speeds, and transfer velocities must be applied. We performed 12 simulations to estimate the importance of technical model-settings and another 40 simulations to assess the importance of environmental conditions. We also compared a case of CH_4 gas emission from the seafloor west of Svalbard with simulations.

Technical parameters

Bubble shapes are implicitly considered in the rising speed parameterizations but experiments determining the gas transfer velocities have not addressed bubble shapes and the increased bubble surface of non-spherical bubbles. This analysis showed that applying flat bubble parameterizations

reduced the rise height of gas by 22% for 6mm bubbles and by 5% for 3mm bubbles. TVM no. 3, based on surfactant-covered bubbles, increased the flare height so much that bubbles reached the surface even in our 400-meter deep model. Such high bubble streams are not observed in an environment outside the CH₄ hydrate stability field. Clean bubble TVM simulations produced dissolved CH₄ profiles well correlated ($r \geq 0.90$) with CH₄-profiles observed during the CAGE 15-6 cruise. As the other applied TVMs resulted in deviating CH₄ profiles, we suggest that, for future simulations of Arctic seafloor emissions of CH₄ bubbles, a clean bubble TVM should be used.

Environmental parameters

Varying ambient dissolved gas profiles have little effect on the resulting CH₄ profiles. Only an unlikely tenfold increase of Nitrogen noticeably altered the rise-height of CH₄ and neglecting dissolved Argon gas has no effect on the resulting profiles. Consequently, we suggest that M2PG1 users may assume that dissolved gases are initially in equilibrium with the atmosphere. The resulting vertical distribution of dissolved CH₄ is highly dependent on the initial bubble size and plume heights are roughly 60% lower when using small bubbles and 90% higher when large bubbles are assumed. We therefore stress the importance of acquiring an in-situ bubble size distribution. High salinity causes bubbles to rise higher due to the lower solubility in saline water but the response in flare height caused by temperature is limited to a few meters. Simulations show that both MO_x and vertical mixing within plausible ranges can be neglected in a seepage region with high water velocity. However, MO_x and vertical mixing may still be important for the fate of CH₄ away from the sources on ocean basin scales.

Model comparison with observations

M2PG1 reproduced well ($r > 0.9$ and $\text{RMSD} < 0.02 \mu\text{mol kg}^{-1}$) the observed dissolved CH₄ profiles acquired during the CAGE 15-6 cruise, using the BSD observed in the area in 2011 and 2012. Ideally, the simulated profile shapes should have a sharper decrease upwards. Such profiles resulted from simulations using smaller initial bubble sizes. Simulated free gas reached heights consistent with most of the flares seen in the echograms acquired during the same research cruise. However, the most prominent flares, reaching over 150 m above the seafloor, were higher than the model simulations (12.0 – 12.8) predicted. This could be attributed to larger bubble sizes or upwelling caused by intense bubble release. We did not observe enough evidence for small-scale upwelling to explain the extra flare height: The buoyancy frequency was only slightly imaginary ($N^2 \in [-0.5 \times 10^{-6}, 0]$) between the seafloor and up to 20 meters above, in stations 1619 and 1620. When a Gaussian BSD peaking at 6 mm was applied, TS values obtained from simulations suggest that flares should be observable up to 167 m above the seafloor, which matches the highest observed flares. As no upwelling due to bubbles has been observed in the area previously (Sahling et al., 2014), we explain the highest flares with bubble sizes larger than the ones previously observed.

Future use and developments

M2PG1 resolves free and dissolved gas dynamics in shallow to moderately deep aquatic environments, and the depth-limitation is currently given by the depth of the pressure-, temperature-, and salinity dependent hydrate stability zones (HSZs). In order to apply the model at deeper sites, including depths within the HSZs, future versions of M2PG1 should include TVMs and BRSMs for hydrate-coated bubbles, and possibly model growth and dissociation of hydrates on bubble skins and the subsequent effect on gas transfer and bubble rising speeds.

The application of M2PG1 targeting methane seepage from the seafloor provides a basis for future incorporation in three-dimensional ocean models, facilitating prediction of 3-dimensional distribution of methane emissions to the atmosphere.

Future versions of M2PG1 could potentially include the carbonate system similarly to Liang et al., (2011), which would allow for direct simulations of local ocean acidification caused by CH₄ seeps. Alternatively, PROBE's capability of coupling ocean basins may be used to quantify ocean acidification from bubble emissions (CO₂ and/or CH₄ bubbles) on ocean basin scales.

In order to predict the vertical distribution of gas at sites where bubble emission is very intense, bubble-driven upwelling could be incorporated, and may be predicted from the number density and drag of buoyant bubbles on the water.

Newly developed acoustic instruments providing broadband signals could facilitate determination of bubble sizes by inverse acoustic modelling of BSD by remote methods. This would greatly simplify the determination of BSDs, which is important for predicting the vertical distribution of CH₄ emitted from the seafloor.

Although the main interest of this study was related to CH₄, a consequence of the coupled gas system is that, once a process-based model is established, it inevitably provides insight to the evolution of all the present gas species, both in their free and dissolved phases. For example, re-distribution of dissolved CO₂ and O₂ due to CH₄ bubbles can be assessed. The effect of bubbles injected to surface waters by wave action and the fate of gas leakage from industrial seafloor installations can be understood from the same process-based model.

Acknowledgements

This work was supported by the Research Council of Norway through its Centres of Excellence funding scheme, project number 223259. We would like to thank the crew on board R/V Helmer Hanssen for the support during the CAGE 15-6 cruise and the cruise leader Jürgen Mienert. A dataset comprising the executable file, simulation settings and results was deposited in the UiT Open Research Data repository <https://doi.org/10.18710/LS2KUX>

References

- Al Zaitone, B. 2018. Evaporation of oblate spheroidal droplets: A theoretical analysis. *Chem. Eng. Commun.* 205: 110-121, doi: 10.1080/00986445.2017.1374949
- Angelis, M. A., and M. I. Scranton. 1993. Fate of methane in the Hudson River and estuary. *Global Biogeochem. Cycles* 7: 509-523, doi: 10.1029/93GB01636
- Biaostoch, A., T. Treude, L. H. Rüpke and others. 2011. Rising Arctic Ocean temperatures cause gas hydrate destabilization and ocean acidification. *Geophys. Res. Lett.* 38, doi: 10.1029/2011GL047222
- Blanchard, D. C. 1989. The ejection of drops from the sea and their enrichment with bacteria and other materials: A review. *Estuaries* 12: 127-137, doi: 10.2307/1351816
- Boetius, A., and F. Wenzhöfer. 2013. Seafloor oxygen consumption fuelled by methane from cold seeps. *Nat. Geosci.* 6: 725-734, doi: 10.1038/ngeo1926
- Carlsson, B., A. Rutgersson, and A.-S. Smedman. 2009. Investigating the effect of a wave-dependent momentum flux in a process oriented ocean model. *Boreal Environ. Res.* 14, doi: 10.1007/s11274-015-1903-5
- Collins, G. L., M. Motarjemi, and G. J. Jameson. 1978. A method for measuring the charge on small gas bubbles. *J. Colloid Interface Sci.* 63: 69-75, doi: 10.1016/0021-9797(78)90036-X
- Damm, E., A. Mackensen, G. Budéus, E. Faber, and C. Hanfland. 2005. Pathways of methane in seawater: Plume spreading in an Arctic shelf environment (SW-Spitsbergen). *Cont. Shelf Res.* 25: 1453-1472, doi: 10.1016/j.csr.2005.03.003
- Delnoij, E., F. Lammers, J. Kuipers, and W. Van Swaaij. 1997. Dynamic simulation of dispersed gas-liquid two-phase flow using a discrete bubble model. *Chem. Eng. Sci.* 52: 1429-1458, doi: 10.1016/S0009-2509(96)00515-5
- Edenhofer, O., R. Pichs-Madruga, Y. Sokona and others. 2014. IPCC, 2014: summary for policymakers. *Mitigation of Climate Change.*
- Edman, M., and A. Omstedt. 2013. Modeling the dissolved CO₂ system in the redox environment of the Baltic Sea. *Limnol. Oceanogr.* 58: 74-92, doi: 10.4319/lo.2013.58.1.0074
- Ferré, B., J. Mienert, and T. Feseker. 2012. Ocean temperature variability for the past 60 years on the Norwegian-Svalbard margin influences gas hydrate stability on human time scales. *J. Geophys. Res.: Oceans* (1978-2012) 117, doi: 10.1029/2012JC008300
- Fofonoff, N. 1985. Physical properties of seawater: A new salinity scale and equation of state for seawater. *J. Geophys. Res.: Oceans* 90: 3332-3342, doi: 10.1029/JC090iC02p03332
- Graves, C. A., L. Steinle, G. Rehder and others. 2015. Fluxes and fate of dissolved methane released at the seafloor at the landward limit of the gas hydrate stability zone offshore western Svalbard. *J. Geophys. Res.: Oceans* 120: 6185-6201, doi: 10.1002/2015JC011084
- Gustafsson, N., L. Nyberg, and A. Omstedt. 1998. Coupling of a high-resolution atmospheric model and an ocean model for the Baltic Sea. *Mon. Weather Rev.* 126: 2822-2846, doi: 10.1175/1520-0493(1998)126%3C2822:COAHRA%3E2.0.CO;2
- Hansson, D., and A. Omstedt. 2008. Modelling the Baltic Sea ocean climate on centennial time scale: temperature and sea ice. *Climate Dynamics* 30: 763-778, doi: 10.1007/s00382-007-0321-2
- Johansen, Ø. 2000. DeepBlow – a Lagrangian Plume Model for Deep Water Blowouts. *Spill Sci. Technol. Bull.* 6: 103-111, doi: doi.org/10.1016/S1353-2561(00)00042-6
- Kirschke, S., P. Bousquet, P. Ciais and others. 2013. Three decades of global methane sources and sinks. *Nat. Geosci.* 6: 813-823, doi: 10.1038/ngeo1955
- Leblond, I., C. Scalabrin, and L. Berger. 2014. Acoustic monitoring of gas emissions from the seafloor. Part I: quantifying the volumetric flow of bubbles. *Mar. Geophys. Res.* 35: 191-210, doi: 10.1007/s11001-014-9223-y
- Leifer, I., J. F. Clark, and R. F. Chen. 2000. Modifications of the local environment by natural marine hydrocarbon seeps. *Geophys. Res. Lett.* 27: 3711-3714, doi: 10.1029/2000GL011619
- Leifer, I., and R. K. Patro. 2002. The bubble mechanism for methane transport from the shallow sea bed to the surface: A review and sensitivity study. *Cont. Shelf Res.* 22: 2409-2428, doi: 10.1016/S0278-4343(02)00065-1

- Liang, J. H., J. C. McWilliams, P. P. Sullivan, and B. Baschek. 2011. Modeling bubbles and dissolved gases in the ocean. *J. Geophys. Res.: Oceans* (1978-2012) 116, doi: 10.1029/2010JC006579
- Luff, R., K. Wallmann, and G. Aloisi. 2004. Numerical modeling of carbonate crust formation at cold vent sites: significance for fluid and methane budgets and chemosynthetic biological communities. *Earth Planet. Sci. Lett.* 221: 337-353, doi: 10.1016/S0012-821X(04)00107-4
- Magen, C., L. L. Lapham, J. W. Pohlman, K. Marshall, S. Bosman, M. Casso, and J. P. Chanton. 2014. A simple headspace equilibration method for measuring dissolved methane. *Limnol. Oceanogr.: Methods* 12: 637-650, doi: 10.4319/lom.2014.12.637
- Mau, S., M. Römer, M. E. Torres and others. 2017. Widespread methane seepage along the continental margin off Svalbard—from Bjørnøya to Kongsfjorden. *Sci. Rep.* 7: 42997, doi: 10.1038/srep42997
- McGinnis, D., J. Greinert, Y. Artemov, S. Beaubien, and A. Wüest. 2006. Fate of rising methane bubbles in stratified waters: How much methane reaches the atmosphere? *J. Geophys. Res.: Oceans* (1978-2012) 111, doi: 10.1029/2005JC003183
- Myhre, C. L., B. Ferré, S. M. Platt and others. 2016. Extensive release of methane from Arctic seabed west of Svalbard during summer 2014 does not influence the atmosphere. *Geophys. Res. Lett.* 43: 4624-4631, doi: 10.1002/2016GL068999
- Omstedt, A. 2011. Guide to process based modeling of lakes and coastal seas. Springer.
- Omstedt, A., and J. S. Wettlaufer. 1992. Ice growth and oceanic heat flux: Models and measurements. *J. Geophys. Res.: Oceans* 97: 9383-9390, doi: 10.1029/92JC00815
- Pachauri, R. K., M. R. Allen, V. R. Barros and others. 2014. Climate change 2014: synthesis report. Contribution of Working Groups I, II and III to the fifth assessment report of the Intergovernmental Panel on Climate Change. IPCC.
- Panieri, G., S. Bünz, D. J. Fornari and others. 2017. An integrated view of the methane system in the pockmarks at Vestnesa Ridge, 79° N. *Mar. Geol.* 390: 282-300, doi: 10.1016/j.margeo.2017.06.006
- Randelhoff, A., A. Sundfjord, and M. Reigstad. 2015. Seasonal variability and fluxes of nitrate in the surface waters over the Arctic shelf slope. *Geophys. Res. Lett.* 42: 3442-3449, doi: 10.1002/2015GL063655
- Rehder, G., P. W. Brewer, E. T. Peltzer, and G. Friederich. 2002. Enhanced lifetime of methane bubble streams within the deep ocean. *Geophys. Res. Lett.* 29, doi: 10.1029/2001GL013966
- Ruppel, C. D., and J. D. Kessler. 2016. The Interaction of Climate Change and Methane Hydrates. *Rev. Geophys.*, doi: 10.1002/2016RG000534
- Sahling, H., M. Römer, T. Pape and others. 2014. Gas emissions at the continental margin west of Svalbard: mapping, sampling, and quantification. *Biogeosciences* 11: 6029-6046, doi: 10.5194/bg-11-6029-2014
- Sam, A., C. Gomez, and J. Finch. 1996. Axial velocity profiles of single bubbles in water/frother solutions. *Int. J. Miner. Process.* 47: 177-196, doi: 10.1016/0301-7516(95)00088-7
- Sauter, E. J., S. I. Muyakshin, J.-L. Charlou and others. 2006. Methane discharge from a deep-sea submarine mud volcano into the upper water column by gas hydrate-coated methane bubbles. *Earth Planet. Sci. Lett.* 243: 354-365, doi: 10.1016/j.epsl.2006.01.041
- Shakhova, N., I. Semiletov, I. Leifer and others. 2014. Ebullition and storm-induced methane release from the East Siberian Arctic Shelf. *Nat. Geosci.* 7: 64-70, doi: 10.1038/ngeo2007
- Shakhova, N., I. Semiletov, A. Salyuk, V. Yusupov, D. Kosmach, and Ö. Gustafsson. 2010. Extensive Methane Venting to the Atmosphere from Sediments of the East Siberian Arctic Shelf. *Science* 327: 1246-1250, doi: 10.1126/science.1182221
- Sloan, E. D., and C. Koh. 2007. Clathrate hydrates of natural gases. CRC press.
- Stepanenko, V. M., E. E. Machul'skaya, M. V. Glagolev, and V. N. Lykossov. 2011. Numerical modeling of methane emissions from lakes in the permafrost zone. *Izv., Acad. Sci., USSR, Atmos. Oceanic Phys.* 47: 252-264, doi: 10.1134/s0001433811020113
- Svensson, U. 1978. A mathematical model of the seasonal thermocline.
- Svensson, U., and A. Omstedt. 1998. Numerical simulations of frazil ice dynamics in the upper layers of the ocean. *Cold Reg. Sci. Technol.* 28: 29-44, doi: 10.1016/S0165-232X(98)00011-1
- Taylor, K. E. 2001. Summarizing multiple aspects of model performance in a single diagram. *J. Geophys. Res.: Atmos.* 106: 7183-7192, doi: 10.1029/2000JD900719

- Uhlig, C., and B. Loose. 2017. Using stable isotopes and gas concentrations for independent constraints on microbial methane oxidation at Arctic Ocean temperatures. *Limnol. Oceanogr.: Methods* 15: 737-751, doi: 10.1002/lom3.10199
- Valentine, D. L., D. C. Blanton, W. S. Reeburgh, and M. Kastner. 2001. Water column methane oxidation adjacent to an area of active hydrate dissociation, Eel River Basin. *Geochim. Cosmochim. Acta* 65: 2633-2640, doi: 10.1016/S0016-7037(01)00625-1
- Veloso, M., J. Greinert, J. Mienert, and M. De Batist. 2015. A new methodology for quantifying bubble flow rates in deep water using splitbeam echosounders: Examples from the Arctic offshore NW-Svalbard. *Limnol. Oceanogr.: Methods* 13: 267-287, doi: 10.1002/lom3.10024
- Vielstädte, L., J. Karstens, M. Haeckel and others. 2015. Quantification of methane emissions at abandoned gas wells in the Central North Sea. *Mar. Pet. Geol.*, doi: 10.1016/j.marpetgeo.2015.07.030
- Wanninkhof, R. 1992. Relationship between wind speed and gas exchange over the ocean. *J. Geophys. Res.: Oceans* (1978-2012) 97: 7373-7382, doi: 10.1029/92JC00188
- Wanninkhof, R. 2014. Relationship between wind speed and gas exchange over the ocean revisited. *Limnol. Oceanogr.: Methods* 12: 351-362, doi: 10.4319/lom.2014.12.351
- Westbrook, G., S. Chand, G. Rossi and others. 2008. Estimation of gas hydrate concentration from multi-component seismic data at sites on the continental margins of NW Svalbard and the Storegga region of Norway. *Mar. Pet. Geol.* 25: 744-758, doi: 10.1016/j.marpetgeo.2008.02.003
- Westbrook, G. K., K. E. Thatcher, E. J. Rohling and others. 2009. Escape of methane gas from the seabed along the West Spitsbergen continental margin. *Geophys. Res. Lett.* 36, doi: 10.1029/2009GL039191
- Woolf, D. K. 1993. Bubbles and the air-sea transfer velocity of gases. *Atmos.-Ocean* 31: 517-540, doi: 10.1080/07055900.1993.9649484
- Wunsch, C., and R. Ferrari. 2004. Vertical mixing, energy, and the general circulation of the oceans. *Annu. Rev. Fluid Mech.* 36: 281-314, doi: 10.1146/annurev.fluid.36.050802.122121
- Zheng, L., and P. D. Yapa. 2002. Modeling gas dissolution in deepwater oil/gas spills. *J Mar Syst* 31: 299-309, doi: 10.1016/S0924-7963(01)00067-7

SI.1 List of symbols and annotations

Symbols, annotations, and indices used in this study including units and typical values, where applicable.

Symbol/ Notation	Meaning	Units in manuscript	Value(s) used in this study	Units in M2PG1
a	Semi-major axis of bubble	[mm]	0 – 10	[m]
A	Horizontal domain area	[m ²]	1800	[m ²]
A_{BS}	Bubble surface area	[mm ²]	Calculated	[m ²]
b	Semi-minor axis of bubble	[mm]	0 – 10	[m]
Ca	Atmospheric equilibrium concentration	[$\mu\text{mol kg}^{-1}$]	Calculated	[$\mu\text{mol kg}^{-1}$]
C_{eq}	Bubble equilibrium concentration	[$\mu\text{mol kg}^{-1}$]	Calculated	[$\mu\text{mol kg}^{-1}$]
C_{SW}	Gas concentration	[$\mu\text{mol kg}^{-1}$]	Calculated	[$\mu\text{mol kg}^{-1}$]
C_B	Boundary concentration	[$\mu\text{mol kg}^{-1}$]	Initial	[$\mu\text{mol kg}^{-1}$]
D	Diffusivity (for transfer velocity)	[cm ² s ⁻¹]	Calculated	[m ² s ⁻¹]
f	Bubble flatness	[]	Calculated	[]
F_d	Drag force	[N]	Calculated	[N]
F	Gas flux to the atmosphere	[mol m ⁻² s ⁻¹]	Calculated	[mol m ⁻² s ⁻¹]
k_A	Transfer velocity (ocean to atmosphere)	[m s ⁻¹]	Calculated	[m s ⁻¹]
k_{MOx}	Oxidation rate constant	[d ⁻¹]	0 – 10	[s ⁻¹]
k_T	Bubble transfer velocity bubble gas	[cm s ⁻¹]	Calculated	[m s ⁻¹]
n	Gas content	[mol]	Calculated	[mol]
$\partial n_R / \partial t$	Gas content change from moving bubbles	[mol s ⁻¹]	Calculated	[mol s ⁻¹]
$\partial n_D / \partial t$	Gas content change from dissolution	[mol s ⁻¹]	Calculated	[mol s ⁻¹]
$\partial n_B / \partial t$	Gas content change from boundaries	[mol s ⁻¹]	Calculated	[mol s ⁻¹]

$NGAS$	Number of modeled gases	[]	5	[]
$NSBIN$	Number of bubble size bins	[]	37	[]
N_Z	Number of vertical bins	[]	400	[]
N^2	Buoyancy frequency squared	[s ⁻²]	Calculated	Not used
P_{ATM}	Atmospheric pressure	[Pa]	101325	[Pa]
P_B	Total pressure inside bubble	[Pa]	Calculated	[Pa]
P_H	Hydrostatic pressure	[Pa]	Calculated	[Pa]
P_{ST}	Surface tension pressure	[Pa]	Calculated	[Pa]
Q_{AF}	Bubble gas escape to atmosphere	[mol s ⁻¹]	Calculated	[mol s ⁻¹]
Q_{AEQ}	Gas emission to atmosphere due to equilibration	[mol s ⁻¹]	Calculated	[mol s ⁻¹]
Q_{EF}	Free gas emission to the water column (from the seafloor)	[mol s ⁻¹]	Calculated	[mol s ⁻¹]
r_E	Equivalent bubble radius	[mm]	0 – 9	[m]
res	Model residual error	[mol]	Calculated	[mol]
S	Solubility	[mol kg ⁻¹]	Calculated	mol kg ⁻¹
S_G	Source/sink, gas moving between bubble sizes	[mol]	Calculated	[mol]
Sc	Schmidt number	[]	Calculated	[]
t	Time	[s]		[s]
u	Water current	[m s ⁻¹]	0 – 30	[m s ⁻¹]
U	Wind speed at 10 meters above the seafloor	[cm s ⁻¹]	5	[m s ⁻¹]
V	Bubble volume	[mm ³]	Calculated	[m ³]
V_M	Molar volume of gas	[m ³ mol ⁻¹]	Calculated	[m ³ mol ⁻¹]
$\frac{\partial V_D}{\partial t}$	Volume change due to dissolution/exsolution	[m ³ s ⁻¹]	Calculated	[m ³ s ⁻¹]

$\frac{\partial V_{PT}}{\partial t}$	Volume change due to pressure/temperature	[m ³ s ⁻¹]	Calculated	[m ³ s ⁻¹]
w_B	Bubble rising speed	[cm s ⁻¹]	0 – 30	[cm s ⁻¹]
X	Molar fraction of free gas in bubbles	[]	Calculated	[]
z	Depth	[m]	0 – 400	[m]
α	Angular eccentricity of bubble	[]	Calculated	[]
δt	Time step of model simulation	[s]	0.0625	[s]
Δt	Result output interval	[s]	600	[s]
ΔV_B	Volume difference of bubble sizes	[mm ³]	Calculated	[m ³]
δ_z	Vertical bin size	[m]	1	[m]
Γ	Vertical mixing coefficient	[m ² s ⁻¹]	$10^{-4} - 10^4$	[m ² s ⁻¹]
ρ_{SW}	Seawater density	[kg m ⁻³]	Calculated	[kg m ⁻³]
σ	Surface tension	[N m ⁻¹]	0.074	[N m ⁻¹]
θ^j	Source term, dissolved gas species	[mol kg ⁻¹ s ⁻¹]	Calculated	[mol kg ⁻¹ s ⁻¹]
μ_{SW}	Seawater dynamic viscosity	[Pa s]	Calculated	[Pa s]
ν_{SW}	Seawater kinematic viscosity	[m ² s ⁻¹]	Calculated	[m ² s ⁻¹]
i	Index for depth (subscript)	[]		
j	Index for gas species (superscript)	[]		
k	Index for bubble size (subscript)	[]		
surf	Index for surface (subscript)	[]		
bot	Index for bottom (subscript)	[]		

SI.2 Bubble rising speed models in M2PG1

Several bubble rising speed models (BRSMs) exist in the literature, all assuming that the terminal velocity, when buoyancy and frictional forces balance, occurs within milliseconds after the initial release, and so there is no need to resolve acceleration of bubbles. The resulting bubble rising speeds predicted by all the models included in M2PG1 depend mainly on the bubble size, but also on water properties (temperature, density and viscosity) and the surface tension. For speed calculations, the bubble radius, r is taken as the equivalent bubble radius, the water density, ρ_{sw} , and viscosity, μ_{sw} are calculated from salinity and temperature and the surface tension σ is taken as a constant in these calculations.

M2PG1 includes a FORTRAN case structure including the nine BRSMs to facilitate a user-chosen model via the initialization file. The BRSMs incorporated in M2PG1 are seen in table SI.3 and detailed here. Figure SI.1 shows the resulting rising speeds from the nine BRSMs at 20°C.

Fan and Tsuchiya, 1990

Leifer and Patro (2002) modified the formula developed by Fan and Tsuchiya (1990) for the rising speeds and suggested the formula:

$$w_b = \left(\left(\frac{\rho_{sw} g r^2}{3.68 M^{-0.038} \mu_{sw}} \right)^{-d} + \left(\frac{c \sigma}{\rho_{sw} r} + g r \right)^{-\frac{d}{2}} \right)^{-\frac{1}{d}}$$

, where the dimensionless Morton number, $M = \frac{g \mu_{sw}^4}{\rho_{sw} \sigma^3}$, the empirically derived coefficient, c was 1.4 for seawater and 1.2 for freshwater. The coefficient, d varied between 0.8 for surfactant-covered bubbles and 1.6 for clean bubbles. M2PG1 uses $c = 1.4$ and $d = 1.6, 1.2$ and 0.8 for BRSMs 1, 3 and 9 respectively.

Woolf and Thorpe, 1991

Woolf and Thorpe (1991) predicted velocities of clean and dirty bubbles and suggest a shift in behaviour at 80-150 micrometres. Equations 10 – 11 in their work gives a parameterization of the rising velocity of clean, small, and large bubbles;

$$w_b = \frac{r^2 g}{3 \nu_{sw}} \quad | \quad r < 80 \mu m$$

$$w_b = \frac{r^2 g}{v_{SW}} \left(18 \left[1 - \frac{2}{\left[1 + (1 + 0.091\chi)^{\frac{1}{2}} \right]} \right] \right)^{-1} \quad | r > 150\mu m$$

Here $\chi = gr^3/v_{SW}^2$ with $v_{SW} = \frac{\mu_{SW}}{\rho_{SW}}$. Rising velocities for bubbles with radius $>80 \mu m$ and $<150 \mu m$ are linearly interpolated between the 80 and 150 μm velocities. Authors report on bubble velocities for bubbles sizes up to 500 μm . The authors also give equations (12 and 13 in their paper) for rising speed of surfactant-covered bubbles:

$$w_b = (2r^2 g/9v_{SW}) \left[(y^2 + 2y)^{\frac{1}{2}} - y \right]$$

$$w_b = \frac{r^2 g}{v_{SW}} \left(18 \left[1 - \frac{2}{\left[1 + (1 + 0.091\chi)^{\frac{1}{2}} \right]} \right] \right)^{-1} \quad | r > 150\mu m$$

Where $y = 10.82\chi$

M2PG1 uses equations 10 – 11 for BRSM no. 2 and 12 – 13 for BRSM no. 8.

Leifer & Patro, 2002

Leifer and Patro (2002) reports (equation 16 in their study) on a simple polynomial parameterization for surfactant-covered bubbles, based on a regression of observed data from (Clift et al., 1978):

$$w_b = 276r - 1648r^2 + 4882r^3 - 7429r^4 + 5618r^5 - 1670r^6$$

M2PG1 uses this parameterization in BRSM no. 4.

Leifer, 2000

Leifer et al. (2000b) suggest that the rising speed is temperature-dependent and give the rising speeds for large, clean bubbles:

$$w_b = A \frac{2cgr^d}{9v_{SW}^n} + B [V_{Bm} + H(r - r_c)^{m2} e^{K(r-r_c)^{m1T}}]$$

$$A = \frac{1}{4} \left[1 + \tanh \left(\frac{T_P - T}{\chi_T} \right) \right] \left[1 + \tanh \left(\frac{r_P - r}{\chi_r} \right) \right]$$

$$B = \frac{1}{4} \left[1 + \tanh \left(\frac{T - T_P}{\chi_T} \right) \right] \left[1 + \tanh \left(\frac{r - r_P}{\chi_r} \right) \right]$$

Here, A and B are hyperbolic transition functions to comply with both non-oscillating and oscillating bubbles. Here the coefficients $K=4.79 \times 10^{-4}$, $H=0.733$, $r_c=0.0584$ cm, $V_{Bm}=22.16$ cm s⁻¹, $m1=-0.815$, and $m2=-0.849$ were determined from regression. The transition points are determined by $r_p = 1086 - 16.05T_p$ and the transition widths are: $\chi_r = 0.0015$ cm, $\chi_T = 2^\circ C$. This parameterization is used in BRSM no 6.

Leifer, surfactant covered bubbles with temperature dependence

BRSM no. 5 uses rising speed data supplied in a Matlab® code by Ira Leifer for inclusion in Veloso et

al. (2015) with additional temperature dependence which affects the rising speed by $w_b = \frac{w_{b20} v_{SW}^{T_{dep}}}{0.0098^{T_{dep}}}$,

where w_{b20} is the observed data at 20°C and

$$T_{dep} = \begin{pmatrix} -0.5 & r < 60 \mu m \\ -0.54 & 60 < r < 320 \mu m \\ -0.64 & r > 320 \mu m \end{pmatrix}. \text{ The underlying velocity data is found in table SI.}$$

Woolf, 1993

Woolf (1993) worked on ocean surface bubble-enhanced gas exchange and found an approximate bubble rising velocity for both clean and surfactant-covered bubbles:

$$wb = 0.172r^{1.28}g^{0.76}v_{SW}^{-0.56} \quad | \quad (wb < 0.25 \text{ ms}^{-1})$$

$$wb = 0.25 \text{ ms}^{-1} \quad | \quad (\text{large bubbles})$$

This parametrization is used in BRSM no. 7, which is the reference BRSM in this study.

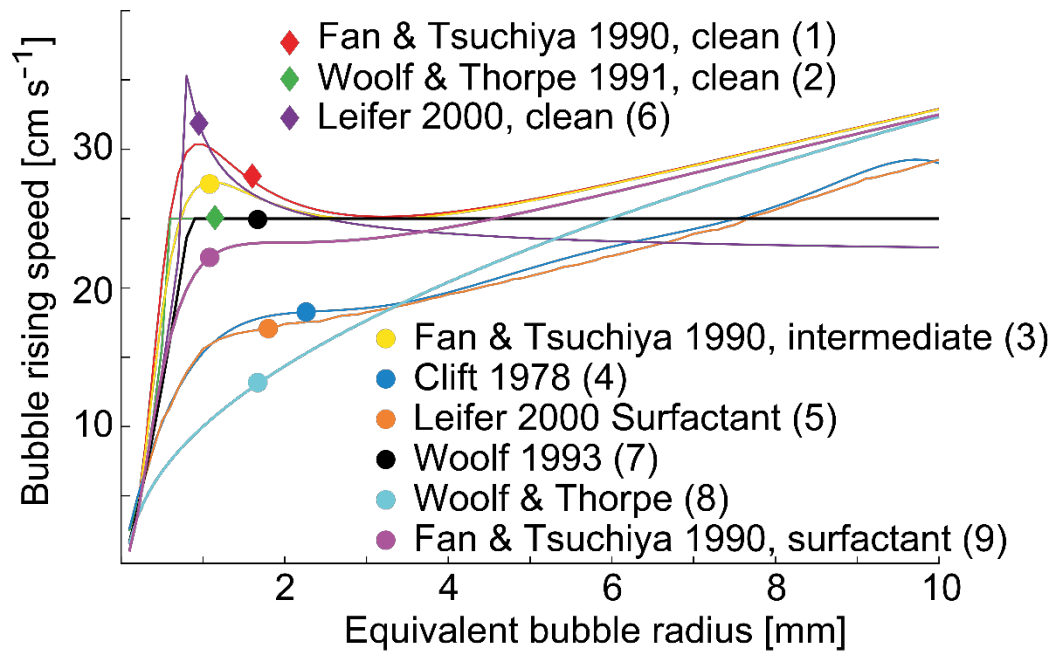


Figure SI.1. Bubble rising speeds as functions of the equivalent bubble radius. Diamonds indicate clean bubble models and dots specify models for surfactant-covered or partially covered bubbles. Colour coding matches Figure 5 in the main manuscript and numbers in parenthesis represents the BRSM no.

Table SI.1. References for M2PG1-implemented Solubility, Molar volume and Diffusivity

Species	Solubility	Molar volume	Diffusivity
N ₂	Mao and Duan (2006)	Mao and Duan (2006)	Hayduk and Laudie (1974)
O ₂	Geng and Duan (2010)	Schmidt and Wagner (1985)	Boudreau (1997)
CO ₂	Duan et al (2006) ¹ Tishchenko et al. (2009) ²	Duan and Sun (2003)	Boudreau (1997)
CH ₄	Kossel et al. (2013) ³ Tishchenko et al. (2005) ⁴	Duan and Mao (2006)	Jähne et al. (1987)
Ar	Hamme & Emerson, (2004) ⁵	Weast (1972)	Jähne et al. (1987)

¹ Outside the CO₂-HSZ; ² Within the CO₂-HSZ.

³ Outside the CH₄-HSZ; ⁴ Within the CH₄-HSZ; ⁵ Extrapolated to high pressure.

Table SI.2. Structure of initial and boundary conditions for M2PG1 simulations. Index 1 is the first water cell above the seafloor.

Index	Temp °C	Salinity PSU	N ₂ μmol kg ⁻¹	O ₂ μmol kg ⁻¹	CO ₂ μmol kg ⁻¹	CH ₄ μmol kg ⁻¹	Ar μmol kg ⁻¹
1	4	35	680	250	25	0.01	0.14
2	4	35	680	250	25	0.01	0.14
3	4	35	680	250	25	0.01	0.14
4	4	35	680	250	25	0.01	0.14
5	4	35	680	250	25	0.01	0.14
6	4	35	680	250	25	0.01	0.14
7	4	35	680	250	25	0.01	0.14
.
.
.
398	4	35	680	250	25	0.01	0.14
399	4	35	680	250	25	0.01	0.14
400	4	35	680	250	25	0.01	0.14

Only numeric values (no headings or units) are supplied in the .txt file

Table SI.3. BRSM's incorporated in M2PG1. The size range within which the BRSM is appropriate and the type of bubble (i.e. bubble rims with a surfactant or clean bubble rims) are indicated.

BRSM	Reference	Range	Bubble type	Comment
1	Fan and Tsuchiya (1990)	0 – 10 mm	Clean	n=1.6 in eq. 2.11
2	Woolf and Thorpe (1991)	0 – 0.5 mm ¹	Clean	Eq. 10, 11

3	Fan and Tsuchiya (1990)	0 – 10 mm	Intermediate	n=1.2 in eq. 2.11
4	Leifer and Patro (2002)	0.6 – 10 mm	Surfactant	Polynomial fit to data (eq. 16)
5	Leifer et al. (2000)	0-4.5 mm	T dependent, Surfactant	Data plus temperature dependence
6	Leifer et al. (2000)	0-4.5 mm	T dependent, Clean	Eq. 10 -17
7	Woolf (1993)	0.1mm – 4mm ¹ .	Both	Eq. 38
8	Woolf and Thorpe (1991)	0 – 0.5 mm ¹ .	Surfactant	Eq. 12, 13
9	Fan and Tsuchiya (1990)	0 – 10 mm	Surfactant	n=0.8 in eq. 2.11

Table SI.4. Output description

File name	Description / Units
M2PG1_FREEGASx.dat ¹	Free gas content (mol) of species x (N ₂ , O ₂ , CO ₂ , CH ₄ , Ar) [Time (h), depth (m), size bin 1, bin 2, ..., bin NSBIN]
M2PG1 DISSOLVEDGASES.dat ¹	Dissolved gas concentrations (μmol kg ⁻¹) [Time (h), depth (m), N ₂ , O ₂ , CO ₂ , CH ₄ , Ar]
M2PG1_bottomsource.dat ²	Source of gas at the source depth (mol) [Time (h), N ₂ , O ₂ , CO ₂ , CH ₄ , Ar]
M2PG1_atm_eq.dat ²	Ocean – Atmosphere equilibration (mol) [Time (h), N ₂ , O ₂ , CO ₂ , CH ₄ , Ar]
M2PG1_atm_fr_gas_esc.dat ²	Ocean - Atmosphere free gas ebullition (mol) [Time (h), N ₂ , O ₂ , CO ₂ , CH ₄ , Ar]
M2PG1_TS.dat ¹	Temperature and salinity. (°C, PSU) [Time (h), depth (m), T, S]

¹ Snapshot of the content/ concentration. Output interval is specified in the .ini file

² Flow quantities, accumulated until written to result-file

Table SI.5. Example BSD

radius [m]	Probability		
0.00001	0	0.0045	0.33784
0.00025	0	0.00475	0.22973
0.0005	0	0.005	0.25676
0.00075	0	0.00525	0.17568
0.001	0.054054	0.0055	0.13514
0.00125	0.081081	0.00575	0.094595
0.0015	0.21622	0.006	0
0.00175	0.39189	0.00625	0
0.002	0.66216	0.0065	0
0.00225	0.74324	0.00675	0.013514
0.0025	0.66216	0.007	0
0.00275	0.75676	0.00725	0
0.003	1	0.0075	0.013514
0.00325	0.90541	0.00775	0
0.0035	0.60811	0.008	0
0.00375	0.41892	0.00825	0
0.004	0.48649	0.0085	0
0.00425	0.41892	0.00875	0
		0.009	0

Table SI.6. Gas mixing ratio of released bubbles

Mixing ratio	Species
0	N ₂
0	O ₂
0	CO ₂
1	CH ₄
0	Ar

Table SI.7. Organization of M2PG1 initialization file

Entry	Explanation
M2PG1_0.0	Simulation name
400	Number of vertical grid cells (N in PROBE)
35	Number of water cells in oceanographic forcing model if transient
1	Type of area (1=vertically same) (INDARE in PROBE)
1800	Area m ² (AREAHZ in PROBE)
400	Water depth (m)
0.0625	Time-step (s) (TFRAC(2) in PROBE)
-1	Last time-step (LSTEP in PROBE) -1 indicates run to steady state
60	Time-steps between output
7	Bubble rising speed model number
2	Bubble flatness (0 for spherical bubbles, 1 for Leblond, 2 for Linear)
1	Gas transfer velocity model number
1	Probe turbulence model (ITURBM in PROBE)
1	Probe type of Prandtl number (IPRSC in PROBE).
1.00E-03	Constant vertical mixing coefficient (m ² s ⁻¹) (EMUCON in PROBE).
1.00E-02	kMOx. Methane oxidation rate constant (d ⁻¹)
0.05	Free gas flow rate in the area (mol s ⁻¹)
0.15	Barotropic current across the boundary (ms ⁻¹) (-999 = dynamic forcing)
'IN\INITIAL400M_simple.txt'	Path to Initial profiles file
'IN\BSD_for_M2PG1_3mm.txt'	Path to Bubble size distribution file (size, probability)
'IN\Gascomposition.txt'	Composition of released gases
0	0= Don't use atmospheric data
"	Path to atmospheric transient boundary condition file
0	0= Don't use transient oceanographic boundary.
"	Path to oceanographic transient boundary file.

Table SI.8a.
Simulation settings

Code	Case focus	# BRSM	Bubble shape	# TVM	Aqueous gas profiles	BSD	Temp °C	Sal. PSU	Flow rate mol s ⁻¹	d-kMOx d ⁻¹	In/ Out flow ms ⁻¹	Mixing coefficient m ² s ⁻¹
0.0	Reference case	7	Linear	1	Atm. eq.	3 mm	4	35	0.05	1.00E-02	0.15	1.00E-03
1.0	Bubble rising speed	1	Linear	1	Atm. eq.	3 mm	4	35	0.05	1.00E-02	0.15	1.00E-03
1.1	Bubble rising speed	2	Linear	1	Atm. eq.	3 mm	4	35	0.05	1.00E-02	0.15	1.00E-03
1.2	Bubble rising speed	3	Linear	1	Atm. eq.	3 mm	4	35	0.05	1.00E-02	0.15	1.00E-03
1.3	Bubble rising speed	4	Linear	1	Atm. eq.	3 mm	4	35	0.05	1.00E-02	0.15	1.00E-03
1.4	Bubble rising speed	5	Linear	1	Atm. eq.	3 mm	4	35	0.05	1.00E-02	0.15	1.00E-03
1.5	Bubble rising speed	6	Linear	1	Atm. eq.	3 mm	4	35	0.05	1.00E-02	0.15	1.00E-03
1.6	Bubble rising speed	8	Linear	1	Atm. eq.	3 mm	4	35	0.05	1.00E-02	0.15	1.00E-03
1.7	Bubble rising speed	9	Linear	1	Atm. eq.	3 mm	4	35	0.05	1.00E-02	0.15	1.00E-03
2.0	Bubble shapes	7	Spheric	1	Atm. eq.	3 mm	4	35	0.05	1.00E-02	0.15	1.00E-03

2.1	Bubble shapes	7	Leblond	1	Atm. eq.	3 mm	4	35	0.05	1.00E-02	0.15	1.00E-03
3.0	Transfer velocity	7	Linear	2	Atm. eq.	3 mm	4	35	0.05	1.00E-02	0.15	1.00E-03
3.1	Transfer velocity	7	Linear	3	Atm. eq.	3 mm	4	35	0.05	1.00E-02	0.15	1.00E-03
4.0	Aqueous gas profiles	7	Linear	1	Half Oxygen	3 mm	4	35	0.05	1.00E-02	0.15	1.00E-03
4.1	Aqueous gas profiles	7	Linear	1	1/100 O ₂	3 mm	4	35	0.05	1.00E-02	0.15	1.00E-03
4.2	Aqueous gas profiles	7	Linear	1	No Ar	3 mm	4	35	0.05	1.00E-02	0.15	1.00E-03
4.3	Aqueous gas profiles	7	Linear	1	Double CO ₂	3 mm	4	35	0.05	1.00E-02	0.15	1.00E-03
4.4	Aqueous gas profiles	7	Linear	1	No N ₂	3 mm	4	35	0.05	1.00E-02	0.15	1.00E-03
4.5	Aqueous gas profiles	7	Linear	1	Double N ₂	3 mm	4	35	0.05	1.00E-02	0.15	1.00E-03
4.6	Aqueous gas profiles	7	Linear	1	Tenfold N ₂	3 mm	4	35	0.05	1.00E-02	0.15	1.00E-03
5.0	Bubble sizes	7	Linear	1	Atm. eq.	1 mm	4	35	0.05	1.00E-02	0.15	1.00E-03
5.1	Bubble sizes	7	Linear	1	Atm. eq.	2 mm	4	35	0.05	1.00E-02	0.15	1.00E-03
5.2	Bubble sizes	7	Linear	1	Atm. eq.	4 mm	4	35	0.05	1.00E-02	0.15	1.00E-03
5.3	Bubble sizes	7	Linear	1	Atm. eq.	6 mm	4	35	0.05	1.00E-02	0.15	1.00E-03
5.4	Bubble sizes	7	Linear	1	Atm. eq.	8 mm	4	35	0.05	1.00E-02	0.15	1.00E-03
6.0	Temperature	7	Linear	1	Atm. eq.	3 mm	0*	35	0.05	1.00E-02	0.15	1.00E-03

6.1	Temperature	7	Linear	1	Atm. eq.	3 mm	1*	35	0.05	1.00E-02	0.15	1.00E-03
6.2	Temperature	7	Linear	1	Atm. eq.	3 mm	2*	35	0.05	1.00E-02	0.15	1.00E-03
6.3	Temperature	7	Linear	1	Atm. eq.	3 mm	3*	35	0.05	1.00E-02	0.15	1.00E-03
6.4	Temperature	7	Linear	1	Atm. eq.	3 mm	6	35	0.05	1.00E-02	0.15	1.00E-03
6.5	Temperature	7	Linear	1	Atm. eq.	3 mm	8	35	0.05	1.00E-02	0.15	1.00E-03
6.6	Temperature	7	Linear	1	Atm. eq.	3 mm	10	35	0.05	1.00E-02	0.15	1.00E-03
6.7	Temperature	7	Linear	1	Atm. eq.	3 mm	20	35	0.05	1.00E-02	0.15	1.00E-03
7.0	Salinity	7	Linear	1	Atm. eq.	3 mm	4	0	0.05	1.00E-02	0.15	1.00E-03
7.1	Salinity	7	Linear	1	Atm. eq.	3 mm	4	20	0.05	1.00E-02	0.15	1.00E-03
7.2	Salinity	7	Linear	1	Atm. eq.	3 mm	4	40	0.05	1.00E-02	0.15	1.00E-03
8.0	Flow rate	7	Linear	1	Atm. eq.	3 mm	4	35	0.025	1.00E-02	0.15	1.00E-03
8.1	Flow rate	7	Linear	1	Atm. eq.	3 mm	4	35	0.1	1.00E-02	0.15	1.00E-03
8.2	Flow rate	7	Linear	1	Atm. eq.	3 mm	4	35	0.15	1.00E-02	0.15	1.00E-03
8.3	Flow rate	7	Linear	1	Atm. eq.	3 mm	4	35	0.2	1.00E-02	0.15	1.00E-03
9.0	Oxidation turnover	7	Linear	1	Atm. eq.	3 mm	4	35	0.05	0	0.15	1.00E-03
9.1	Oxidation turnover	7	Linear	1	Atm. eq.	3 mm	4	35	0.05	0.1	0.15	1.00E-03

9.2	Oxidation turnover	7	Linear	1	Atm. eq.	3 mm	4	35	0.05	1	0.15	1.00E-03
9.3	Oxidation turnover	7	Linear	1	Atm. eq.	3 mm	4	35	0.05	10	0.15	1.00E-03
10.0	Water current	7	Linear	1	Atm. eq.	3 mm	4	35	0.05	1.00E-02	0.025	1.00E-03
10.1	Water current	7	Linear	1	Atm. eq.	3 mm	4	35	0.05	1.00E-02	0.05	1.00E-03
10.2	Water current	7	Linear	1	Atm. eq.	3 mm	4	35	0.05	1.00E-02	0.1	1.00E-03
10.3	Water current	7	Linear	1	Atm. eq.	3 mm	4	35	0.05	1.00E-02	0.2	1.00E-03
10.4	Water current	7	Linear	1	Atm. eq.	3 mm	4	35	0.05	1.00E-02	0.5	1.00E-03
11.0	Mixing coefficient	7	Linear	1	Atm. eq.	3 mm	4	35	0.05	1.00E-02	0.15	1.00E-04
11.1	Mixing coefficient	7	Linear	1	Atm. eq.	3 mm	4	35	0.05	1.00E-02	0.15	1
11.2	Mixing coefficient	7	Linear	1	Atm. eq.	3 mm	4	35	0.05	1.00E-02	0.15	100
11.3	Mixing coefficient	7	Linear	1	Atm. eq.	3 mm	4	35	0.05	1.00E-02	0.15	10000
12.0	Case 15-6 cruise	7	Linear	1	O ₂ CTD	Veloso	CTD	CTD	0.005**	1.00E-02	0.185	1.00E-03
12.1	Case 15-6 cruise	5	Linear	1	O ₂ CTD	Veloso	CTD	CTD	0.005**	1.00E-02	0.185	1.00E-03
12.2	Case 15-6 cruise	8	Linear	1	O ₂ CTD	Veloso	CTD	CTD	0.005**	1.00E-02	0.185	1.00E-03
12.3	Case 15-6 cruise	7	Linear	1	O ₂ CTD	2mm ^	CTD	CTD	0.005**	1.00E-02	0.185	1.00E-03
12.4	Case 15-6 cruise	5	Linear	1	O ₂ CTD	2mm ^	CTD	CTD	0.005**	1.00E-02	0.185	1.00E-03

12.5	Case 15-6 cruise	8	Linear	1	O ₂ CTD	2mm ^	CTD	CTD	0.005**	1.00E-02	0.185	1.00E-03
12.6	Case 15-6 cruise	7	Linear	1	O ₂ CTD	1mm ^	CTD	CTD	0.005**	1.00E-02	0.185	1.00E-03
12.7	Case 15-6 cruise	5	Linear	1	O ₂ CTD	1mm ^	CTD	CTD	0.005**	1.00E-02	0.185	1.00E-03
12.8	Case 15-6 cruise	8	Linear	1	O ₂ CTD	1mm ^	CTD	CTD	0.005**	1.00E-02	0.185	1.00E-03

* Simulations within the CH₄-HSZ; ** Mean single flare flow rate from Flarehunter analysis; ^ Peak radius of Gaussian distribution

Table SI.8b.
Simulation results

Name	plume height 1%	plume height 10%	plume height 20%	Flare height 1%	Flare height 10%	Flare height 20%	COR1	RMSD2	STD3	Max conc
	m	m	m	m	m	m	[]	$\mu\text{mol kg}^{-1}$	$\mu\text{mol kg}^{-1}$	$\mu\text{mol kg}^{-1}$
M2PG1 0.0	83.7	56.6	44.6	88.7	54.6	41.6	1.0000	0.0000	0.0348	0.1851
M2PG1 1.0	88.7	58.6	46.6	89.7	54.6	41.6	0.9997	0.0021	0.0368	0.1929
M2PG1 1.1	86.7	57.6	45.6	88.7	54.6	41.6	0.9999	0.0017	0.0364	0.1913
M2PG1 1.2	85.7	57.6	45.6	88.7	53.6	41.6	1.0000	0.0016	0.0364	0.1924
M2PG1 1.3	71.7	46.6	36.6	72.7	43.6	33.6	0.9912	0.0144	0.0481	0.2782
M2PG1 1.4	59.6	37.6	28.6	61.7	36.6	27.6	0.9639	0.0228	0.0544	0.3473
M2PG1 1.5	88.7	58.6	46.6	88.7	53.6	40.6	0.9998	0.0034	0.0381	0.2008
M2PG1 1.6	63.7	42.6	33.6	66.7	42.6	32.6	0.9829	0.0170	0.0500	0.2916
M2PG1 1.7	80.7	53.6	42.6	83.7	51.6	39.6	0.9994	0.0045	0.0391	0.2111
M2PG1 2.0	88.7	60.7	48.6	92.7	57.6	44.6	0.9982	0.0022	0.0341	0.1700
M2PG1 2.1	83.7	55.6	43.6	88.7	54.6	41.6	0.9999	0.0008	0.0354	0.1906

M2PG1 3.0	189.0	142.9	115.8	218.0	135.8	104.8	0.8241	0.0200	0.0257	0.0987
M2PG1 3.1	195.0	151.9	100.8	NaN	335.3	258.1	0.5710	0.0301	0.0104	0.0454
M2PG1 4.0	84.7	56.6	44.6	88.7	54.6	41.6	1.0000	0.0004	0.0353	0.1868
M2PG1 4.1	83.7	56.6	44.6	88.7	54.6	41.6	1.0000	0.0001	0.0350	0.1856
M2PG1 4.2	83.7	56.6	44.6	88.7	54.6	41.6	1.0000	0.0000	0.0348	0.1851
M2PG1 4.3	84.7	56.6	44.6	88.7	54.6	41.6	1.0000	0.0003	0.0351	0.1863
M2PG1 4.4	82.7	55.6	44.6	85.7	53.6	40.6	1.0000	0.0008	0.0341	0.1819
M2PG1 4.5	84.7	56.6	44.6	91.7	55.6	42.6	1.0000	0.0006	0.0354	0.1876
M2PG1 4.6	96.7	61.7	48.6	123.8	69.7	51.6	0.9986	0.0067	0.0412	0.2119
M2PG1 5.0	31.6	18.5	14.5	35.6	20.6	15.5	0.8113	0.0313	0.0521	0.4293
M2PG1 5.1	56.6	35.6	27.6	61.7	36.6	27.6	0.9579	0.0124	0.0407	0.2635
M2PG1 5.2	106.8	72.7	56.6	112.8	70.7	54.6	0.9896	0.0052	0.0330	0.1644
M2PG1 5.3	140.9	95.7	72.7	149.9	95.7	72.7	0.9569	0.0105	0.0305	0.1403
M2PG1 5.4	163.9	107.8	79.7	176.9	109.8	81.7	0.9434	0.0119	0.0302	0.1368
M2PG1 6.0	100.8	71.7	57.6	103.8	67.7	52.6	0.9850	0.0066	0.0316	0.1491
M2PG1 6.1	93.7	66.7	53.6	97.7	62.7	49.6	0.9924	0.0050	0.0319	0.1554

M2PG1 6.2	87.7	61.7	49.6	91.7	58.6	45.6	0.9970	0.0034	0.0326	0.1633
M2PG1 6.3	85.7	58.6	46.6	89.7	55.6	42.6	0.9993	0.0015	0.0342	0.1752
M2PG1 6.4	85.7	57.6	45.6	89.7	54.6	42.6	1.0000	0.0006	0.0354	0.1868
M2PG1 6.5	84.7	56.6	45.6	89.7	55.6	42.6	1.0000	0.0003	0.0348	0.1843
M2PG1 6.6	84.7	57.6	45.6	90.7	55.6	42.6	1.0000	0.0004	0.0347	0.1833
M2PG1 6.7	87.7	58.6	46.6	92.7	56.6	42.6	0.9998	0.0011	0.0356	0.1867
M2PG1 7.0	71.7	47.6	37.6	74.7	45.6	34.6	0.9946	0.0042	0.0368	0.2058
M2PG1 7.1	77.7	52.6	41.6	82.7	50.6	38.6	0.9988	0.0021	0.0360	0.1970
M2PG1 7.2	86.7	57.6	45.6	90.7	55.6	42.6	0.9998	0.0007	0.0348	0.1828
M2PG1 8.0	83.7	55.6	43.6	88.7	54.6	41.6	1.0000	0.0174	0.0174	0.0976
M2PG1 8.1	83.7	56.6	45.6	88.7	54.6	41.6	1.0000	0.0348	0.0697	0.3602
M2PG1 8.2	84.7	57.6	45.6	88.7	54.6	41.6	1.0000	0.0705	0.1053	0.5386
M2PG1 8.3	84.7	57.6	45.6	88.7	54.6	41.6	1.0000	0.1055	0.1404	0.7145
M2PG1 9.0	83.7	56.6	44.6	88.7	54.6	41.6	1.0000	0.0000	0.0348	0.1851
M2PG1 9.1	83.7	56.6	44.6	88.7	54.6	41.6	1.0000	0.0000	0.0348	0.1851
M2PG1 9.2	83.7	56.6	44.6	88.7	54.6	41.6	1.0000	0.0001	0.0348	0.1848

M2PG1 9.3	83.7	56.6	44.6	88.7	54.6	41.6	1.0000	0.0006	0.0343	0.1818
M2PG1 10.0	80.7	52.6	41.6	88.7	54.6	41.6	0.9987	0.0205	0.0552	0.3007
M2PG1 10.1	81.7	53.6	42.6	88.7	54.6	41.6	0.9992	0.0152	0.0499	0.2703
M2PG1 10.2	82.7	55.6	43.6	88.7	54.6	41.6	0.9998	0.0066	0.0414	0.2216
M2PG1 10.3	84.7	57.6	45.6	88.7	54.6	41.6	0.9999	0.0051	0.0297	0.1573
M2PG1 10.4	88.7	60.7	48.6	88.7	54.6	41.6	0.9975	0.0203	0.0146	0.0790
M2PG1 11.0	83.7	56.6	44.6	88.7	54.6	41.6	1.0000	0.0000	0.0348	0.1851
M2PG1 11.1	83.7	56.6	44.6	88.7	54.6	41.6	1.0000	0.0000	0.0348	0.1847
M2PG1 11.2	85.7	58.6	46.6	88.7	54.6	41.6	0.9992	0.0015	0.0342	0.1700
M2PG1 11.3	170.9	111.8	88.7	88.7	54.6	41.6	0.8981	0.0178	0.0221	0.0871
M2PG1 12.0	133.8	80.7	59.6	125.8	73.7	54.6	0.9810	0.0149	0.0209	0.1054
M2PG1 12.1	86.7	52.6	39.6	84.7	49.6	36.6	0.9969	0.0080	0.0273	0.1582
M2PG1 12.2	105.8	64.7	48.6	104.8	61.7	45.6	0.9976	0.0110	0.0241	0.1289
M2PG1 12.3	105.8	61.7	45.6	99.7	56.6	41.6	0.9985	0.0103	0.0247	0.1367
M2PG1 12.4	68.7	40.6	30.6	66.7	38.6	28.6	0.9738	0.0082	0.0319	0.2055
M2PG1 12.5	77.7	45.6	33.6	76.7	43.6	32.6	0.9866	0.0074	0.0297	0.1827

M2PG1 12.6	85.7	47.6	34.6	83.7	45.6	33.6	0.9873	0.0077	0.0290	0.1809
M2PG1 12.7	58.6	33.6	24.6	57.6	31.6	23.6	0.9392	0.0124	0.0361	0.2562
M2PG1 12.8	62.7	34.6	24.6	62.7	34.6	24.6	0.9459	0.0115	0.0352	0.2471

$${}^1 R = \frac{\sum([C-\bar{C}] \times [C_r - \bar{C}_r])}{N \times STD(C) \times STD(C_r)}; {}^2 RMSD = \sqrt{\frac{\sum([C-\bar{C}] - [C_r - \bar{C}_r])^2}{N}}; {}^3 STD = \sqrt{\frac{\sum([C-\bar{C}]^2)}{N}}. C \text{ is the case value and } C_r \text{ is the reference value}$$

Table SI.9. Bubble rising speed data for BRSM no. 5. 20°C surfactant covered.

radius [cm]	Velocity [cm s ⁻¹]	radius [cm]	Velocity [cm s ⁻¹]	radius [cm]	Velocity [cm s ⁻¹]
0.0025	0.18	0.18	17.1	0.49	20.75
0.005	0.65	0.19	17.2	0.5	20.85
0.0075	1.2	0.2	17.35	0.51	21
0.01	1.7	0.21	17.45	0.52	21.15
0.0125	2.2	0.22	17.5	0.53	21.3
0.015	2.8	0.23	17.6	0.54	21.45
0.0175	3.5	0.24	17.65	0.55	21.6
0.02	4	0.25	17.7	0.56	21.7
0.025	5.4	0.26	17.85	0.57	21.85
0.03	6.4	0.27	17.95	0.58	22
0.035	7.5	0.28	18.05	0.59	22.2
0.04	8.5	0.29	18.1	0.6	22.35
0.045	9.2	0.3	18.25	0.62	22.6
0.05	10.05	0.31	18.35	0.64	22.9
0.055	10.9	0.32	18.45	0.66	23.2
0.06	11.4	0.33	18.55	0.68	23.5
0.065	12.1	0.34	18.7	0.7	23.85
0.07	12.8	0.35	18.8	0.72	24.15
0.075	13.3	0.36	18.95	0.74	24.4
0.08	13.9	0.37	19.1	0.76	24.8
0.085	14.3	0.38	19.25	0.78	25.3
0.09	14.75	0.39	19.35	0.8	25.65
0.095	15.1	0.4	19.5	0.82	26.05
0.1	15.45	0.41	19.65	0.84	26.45
0.11	15.95	0.42	19.75	0.86	26.8
0.12	16.3	0.43	19.85	0.88	27.2
0.13	16.5	0.44	20.05	0.9	27.6
0.14	16.7	0.45	20.2	0.92	28
0.15	16.8	0.46	20.3	0.94	28.25
0.16	16.9	0.47	20.45	0.96	28.55
0.17	17	0.48	20.6	0.98	28.9
				1	29.25